Visible light sensitive mesoporous nanohybrids of lepidocrocite-like ferrititanate coupled to a charge transfer complex: Synthesis, characterization and photocatalytic degradation of NO

Margarita Habran[1], Patricia I. Pontón[2], Lidija Mancic[3], Omar Pandoli[4], Klaus Krambrock[5], Marcelo E. H. Maia da Costa[6], Sonia Letichevsky[1], Antonio M.L.M. Costa[1], Edisson Morgado Jr.[7], Bojan A. Marinkovic[1]*

[1] *Department of Chemical and Materials Engineering, Pontifical Catholic University of Rio de Janeiro, 22451-900, Rio de Janeiro, RJ, Brazil*

[2] *New Materials Laboratory, Department of Materials, Escuela Politécnica Nacional, 170525, Quito, Ecuador*

[3] *Institute of Technical Sciences of SASA, Knez Mihailova 35/IV, Belgrade, Serbia*

[4] *Department of Chemistry, Pontifical Catholic University of Rio de Janeiro, 22451-900, Rio de Janeiro, RJ, Brazil*

[5] *Department of Physics, Federal University of Minas Gerais, 31270-901, Belo Horizonte, Brazil*

[6] *Department of Physics, Pontifical Catholic University of Rio de Janeiro, 22451-900, Rio de Janeiro, RJ, Brazil*

[7] *PETROBRAS S.A., Research & Development Centre, 21941-915, Rio de Janeiro, RJ, Brazil*

*bojan@puc-rio.br

Abstract

The efficiency of photo-oxidation of pollutants catalysed by semiconductors is still limited for real-world applications due to several drawbacks, such as a) insufficient absorption of visible radiation, which predominates in solar spectrum, b) rapid free electron to hole recombination, c) small surface area, built from equilibrium crystallographic facets with low adsorption capacities and d) photo-corrosion. The present study disclosures new mesoporous heterostructures, built from exfoliated lepidocrocite-like ferrititanates and TiO_2 (anatase)-acetylacetone charge transfer complex, capable of reducing free electron-to-hole recombination rate through a robust charge separation and sensitive to the visible light spectrum. The synthesis route is based on soft-chemistry and low temperature calcination at 300°C. Two different partially pillarized heterostructures, denoted as HM-1 and HM-2, have been synthesized. It was observed that the heterostructure HM-1 was four times more active toward photocatalytic degradation of NO gas in comparison to the benchmark photocatalytic material P25. The lower activity of the heterostructure HM-2, comparable to that of P-25, was attributed to the high value of Urbach energy that indicates high number of defect sites within energy band-gap of the constituent semiconductor components. [Ti] anatase/[Ti] ferrititanate mol ratio might also play a role in photocatalytic efficiency.

Keywords: heterostructure; TiO_2-based nanostructures; acetylacetonate; charge separation; air remediation.

1. INTRODUCTION

After pioneering efforts [1-4], the interest in heterogeneous photocatalysis, as an alternative environmental technology, started growing exponentially [1–3]. It was rapidly noticed, however, that the efficiency of photo-oxidation of pollutants catalysed by TiO_2, or by other semiconductors, was still limited for real-world applications due to several drawbacks, such as: **a)** insufficient absorption of visible radiation, that predominates in solar spectrum; **b)** small surface area, built from equilibrium crystallographic facets with low adsorption capacities; **c)** photo-corrosion, in the case of metal sulphides and **d)** rapid free electron to hole recombination.

The tentatives to increase photocatalytic efficiency through charge separation of electron-hole pairs can be traced back in literature, at least, to the paper by Kraeutler and Bard [4], who observed an improvement of photocatalytic activity when TiO_2-anatase particles were platinized. This research has been followed by other studies focused on heterojunctions obtained through coupling of two semiconductors, one with a smaller bandgap, sensitive to visible light, such as CdS, and another with a higher bandgap, such as TiO_2, ZnO or AgI [5–7]. These authors [5,6] observed an increased photocatalytic activity, related to the quenching of the fluorescence of CdS, a phenomenon explained by the free electron injection from the conduction band (CB) of CdS into the CB of the higher bandgap semiconductor, due to its higher redox potential. Furthermore, a proper alignment of the energy bands of the two semiconductors, staggered in these cases, is fundamental for redox reactions be thermodynamically viable and lead to the formation of reactive oxidizing species (ROS), such as $OH^{\bullet}$ and $O_2^{\bullet-}$. Similarly, the benchmark photocatalytic material P25 (Evonik), a mixture of anatase and rutile in a ratio between 70:30 and 85:15, with a variable, and minor, content of amorphous titania [8], owns its photocatalytic activity, higher than the sum of the photocatalytic activities of the individual titania phases, to an efficient charge separation through the injection of excited electrons from the rutile CB into the anatase CB [9].

The idea to design pillared host-guest semiconductor heterojunctions, where the host component presents a layered, bi-dimensional, crystal structure and the guest are fine nanoparticles, occupying interlayer spaces, has been proposed by Sato et al.[10] aiming to enhance dispersion and contacts between the two semiconductors to increase charge separation and to rise porosity and specific surface area of the system allowing a better interaction between the solid photocatalyst and the gas/liquid molecules. The amount of literature on different host/guest arrangements, either micro- or mesoporous, pillared or non-pillared, is respectable nowadays, although the majority of it focuses on the lamellar titanate-TiO_2 heterostructures [15–29]. However, the attempts to synthesize visible-light active photocatalyst through the host/guest strategy are still very rare. Kim et al [21] reported such a tentative through pillaring of a layered titanate, with lepidocrocite-like structure, with the visible-light sensitive CrO_x semiconductor. Such a pillared heterostructure, after calcination at 400°C, presented much higher

photo-degradation of phenol under visible-light irradiation, as compared to the separated components and higher than that obtained with the benchmark photocatalytic material P25.

Different titanate nanostructures can be prepared from low-cost rutile or ilmenite mineral sands [22–25]. When this latter is treated under alkaline hydrothermal conditions at the temperatures ≤ 150°C, ferrititanate nanosheets with lepidocrocite crystal structure are formed [24,25]. These consist, on average, of about 10 to 20 monolayers, providing foils of the thickness of few tens of nanometers, with the lateral dimensions of few hundred of nanometers [26]. Differently from the lepidocrocite layered titanate, which is a high-energy band gap semiconductor (3.8 eV) and does not absorb in the visible part of electromagnetic spectrum [27], lepidocrocite ferrititanate strongly absorbs visible-light, although the exact value of its band-gap energy has not been determined yet [25]. In accordance to Sakai et al., [27] the contact between lepidocrocite titanate nanosheets and anatase particles form a straddled, i.e., type I, heterojunction that can separate charge carriers, due to different rates in charge transfer of electrons and holes from the titanates nanosheets to anatase. In the case of ferrititanate nanosheets, visible light absorption is due to incomplete *d*-shells of Fe^{3+}, forming energy states within the bandgap. Considering the bandgap of lepidocrocite titanates [27], the fully occupied T_{2g} states of Fe^{3+} are localized above valence band (VB) of lepidocrocite ferrititanate, while unoccupied E_g states are positioned below CB [28]. Therefore, excitation of the valence electrons, from fully occupied states of Fe^{3+} to the CB of ferrititanate occurs through the absorption of visible light [29], which is also absorbed by d-d transition and/or charge transfer between interacting ions ($Fe^{3+} + Fe^{3+} = Fe^{2+} + Fe^{4+}$) [28]. The transition from VB to unoccupied E_g states might also contribute to visible light absorption inside ferrititanates.

NO_x is a regulated pollutant, emitted continuously in high ppm concentrations by several industrial stationary units. The development of improved de-NO_x photocatalysts might be an alternative way to attenuate this environmental issue. Huang et al. [30–32] proposed several new and efficient de-NO_x photocatalysts under visible light, such as Bi_2WO_6 as well as heterostructures like $LaFeO_3$-$SrTiO_3$ and $ZnFe_2O_4$-carbon quantum dots. Luévano-Hipólito et al. [33,34] evaluated WO_3 and scheelite-type compounds in

de-NO_x photocatalytic reactions under ultra-violet (UV) radiation. Single phase TiO_2-based materials have also been well evaluated for NO_x degradation [35–39] as well as in heterostructures when combined with other phases, such as WO_3, g-C_3N_4, amorphous carbon or hydroxyapatite [40–43]. Very recently Dong et al., [44] pointed out to a rare earth-abundant insulator ($SrTiO_3$) – semiconductor (BiOI) heterostructure with promising photocatalytic activity in visible light. The same authors designed two new C_3N_4-based visible-light photocatalysts, graphene-like C_3N_4 nanosheets and O/Ba co-functionalized amorphous carbon nitride, both presenting high efficiency toward NO removal, while the second one also promotes suppression of toxic intermediates formation [45,46]. Another C_3N_4-based photocatalysts, MnO_x/C_3N_4, showed high de-NO_x photo-thermal activity in ultraviolet-visible light spectrum [47].

The main goal of the present study is to develop a semiconducting heterostructure that absorbs within visible light spectrum and exhibit high efficiency for photocatalytic NO_x abatement by reducing free electron-to-hole recombination rate through a robust charge separation. The proposed scheme for the charge separation, inside this new heterostructure, is through the injection of free electrons into anatase CB, originating from the highest-occupied-molecular-orbital (HOMO) of acetylacetonate (Acac), linked to anatase, followed by their subsequent injection into unoccupied iron *d*-orbitals (E_g) within ferrititanate band-gap (trapping sites). The visible light sensitivity would be assured through the absorption of ferrititanates, as specified above, and by the formation of the charge transfer complex (CT) between anatase nanoparticles and Acac. A successful synthesis of a CT based on TiO_2 and Acac has been recently reported by Sannino et al., [48]. In order to promote redox reactions, resulting in the formation of ROS, this heterojunction has to present a sufficiently positive redox potential of the photogenerated hole to oxidize H_2O/OH^-, while the redox potential of the photogenerated CB electrons must be sufficiently negative to be able to reduce O_2. The general path towards formation of such a material is summarized in a schematic draw presented in Figure 1. It is worth noting that there are no reports, as far as the authors are aware of, on the use of lepidocrocite ferrititanate nanosheets and anatase-based CT for the preparation of mesoporous nanohybrid heterostructures.

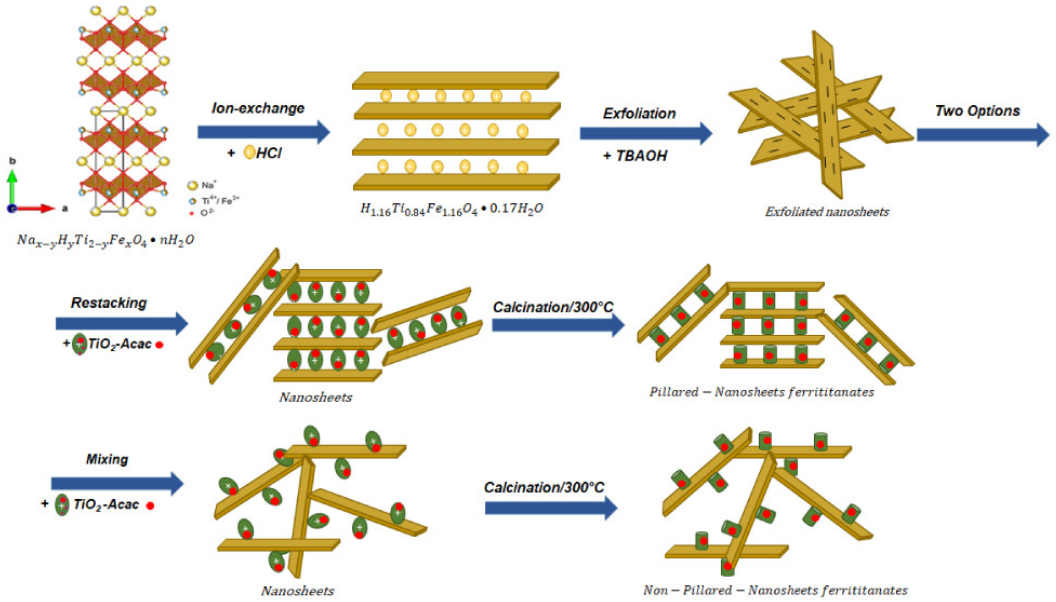

Figure 1. Schematic representation of two possible heterostructures, pillared and non-pillared, potentially obtained from exfoliated lepidocrocite-like ferrititanate nanosheets coupled to anatase-based charge transfer complex, through a soft-chemical route followed by calcination at low temperatures.

2. EXPERIMENTAL

2.1. Materials

Brazilian, ilmenite-rich, mineral sand was used, after proper milling, as precursor for the synthesis of sodium-rich ferrititanate nanosheets under alkaline hydrothermal conditions [49]. Tetrabutylammonium hydroxide (TBAOH), purity ≥ 98%; titanium isopropoxide ($Ti(OiPr)_4$), purity ~97%; acetylacetone, purity ~99%, and ethanol, purity ≥ 99.8%, were purchased from Sigma Aldrich and used as obtained. All other chemicals were of reagent grade.

2.2. Synthesis of exfoliated ferrititanate nanosheets

Sodium-rich lepidocrocite-like ferrititanate nanosheets, $Na_{x-y}H_yTi_{2-x}Fe_xO_4 \cdot nH_2O$, were prepared by alkaline hydrothermal synthesis of ilmenite sand precursor according to the previously published procedure [24]. The corresponding protonic form $H_xTi_{2-x}Fe_xO_4 \cdot nH_2O$ was obtained after a rapid acid-exchange reaction of the sodium-rich nanosheets with 1M HCl aqueous solution at room temperature, during 2 h [26].

The fully protonated nanosheets were exfoliated into individual single-layered sheets using tetrabutylammonium hydroxide (TBAOH) molecules. In a typical procedure, 1 g of fully protonated nanosheets was dispersed into 50 mL of deionized water at 60°C under magnetic stirring for 1 h. In separate, an aqueous

solution of TBAOH was prepared by dissolving 0.27 g of this compound in 50 mL of deionized water at 60°C. The amount of TBAOH was calculated to satisfy TBA^+/H^+ molar ratio of 5 (see Supplementary Material s1) and to assure complete exfoliation [50] considering the cation-exchange capacity of protonated lepidocrocite-like ferrititanate nanosheets (2.1 meq/100g), previously determined by ASTM C837-99. The as-prepared TBAOH aqueous solution was added to the aqueous dispersion of fully protonated nanosheets and the resulting suspension was vigorously mixed using an Ultra-Turrax IKA T25 disperser at 3500 rpm, for 5 h. Finally, the exfoliated ferrititanate nanosheets were recovered as decanted wet material (solids content of 42 wt% measured as demonstrated in figure s1 of Supplementary Material) after centrifugation at 6000 rpm for 20 min and dried at room temperature for further characterization. For the synthesis of the mesoporous nanohybrids (see section 2.4), the exfoliated ferrititanate nanosheets was used as slurry, without drying.

A Perkin-Elmer Optima 7300 DV spectrometer (Inductively Coupled Plasma-Atomic Emission Spectrometer- ICP/AES) and a Perkin-Elmer Simultaneous Thermal Analyzer STA-6000 (Thermogravimetric analysis-TGA), operating under air atmosphere at a heating rate of 10°C min^{-1} within 30-300°C range), were applied to measure Fe/Ti and water weight contents, respectively, aiming to determine chemical formula of the protonated nanosheets. Chemical formula was calculated as $H_{1.16}Ti_{0.84}Fe_{1.16}O_4$ x $0.17H_2O$, as described in details in the s2 Supplementary Material.

2.3. Synthesis of anatase linked with Acac (Charge-transfer complex)

The synthesis of monodispersed and non-aggregated charge-transfer complex was carried out based on the procedures reported by Scolan and Sanchez [51] and Sannino et al., [48]. Firstly, 30 mL of $Ti(OiPr)_4$ were added dropwise to the complexant, an acetylacetone/ethanol solution 1:5 v/v (20 mL of acetylacetone mixed with 100 mL of ethanol), under magnetic stirring. As a result, a yellowish solution was formed. After 40 min of agitation at room temperature, 180 mL of 0.015 M HNO_3 aqueous solution were added dropwise to the stirred yellowish solution to accomplish the hydrolysis reaction. The resulting solution was heated at 60°C for 8 h in order to induce condensation reaction, which led to the formation of a yellow TiO_2-sol. The concentration of TiO_2 in the

as-synthesized TiO_2-sol was 0.307 M (see Supplementary Material s3). The initial complexant/metal ratio (A) was ~2, while the initial hydrolysis (H) and the acidity (H^+) ratios were 100 and 0.027, respectively (see Supplementary Material s4). TiO_2-xerogel was obtained after complete solvent evaporation at room temperature (formation of a red-yellowish TiO_2-xerogel linked with Acac), followed by oven drying at 100°C overnight. TiO_2-xerogel was ground in an agate mortar and stored in a desiccator with silica gel.

2.4. Synthesis of mesoporous nanohybrids

Two nanohybrids were synthesized following the soft-chemical route described by Bai et al [52]. The nominal [Ti] anatase/[Ti] ferrititanate molar ratio of 20 was adopted in the present work.

In the first synthesis, 0.28 g of TiO_2-xerogel with Acac (section 2.3) was re-dispersed by magnetic stirring in 8.8 mL of deionized water. This dispersion was then added dropwise to 40 mL of the aqueous dispersion of exfoliated ferrititanate nanosheets, with a [TiO_2] concentration of 0.29 g/L, under magnetic stirring. The resulting dispersion was heated and kept stirring at 60°C for 24 h. Afterwards, the dispersion was centrifuged at 6000 rpm, for 30 min, and the decanted slurry was washed with an ethanol/water solution (1:1 v/v). The recovered material was dried at room temperature overnight and then calcined at 300°C for 2h to obtain the nanohybrid, denoted as **HM-1**. The resulting calculated [Ti] anatase/[Ti] ferrititanate mol ratio was 19 (Supplementary Material s5).

In the second case, the nanohybrids were synthesized based on the same procedure described above, except for the fact that the TiO_2 sol, as synthesized, was used, not the dried material (xerogel). 12 mL of the TiO_2-sol (0.307 M) was added dropwise into the dispersion of exfoliated ferrititanate nanosheets. The recovered material was dried at room temperature and then calcined at 300°C, and also, at 400°C for 2h. The as-synthesized nanohybrid was named as **HM-2**. The resulting calculated [Ti] anatase/[Ti] ferrititanate mol ratio was 26 (Supplementary Material s5).

2.5. Characterization techniques

2.5.1. Characterization of exfoliated ferrititanate nanosheets

The textural properties of exfoliated ferrititanate nanosheets were determined by N_2 adsorption-desorption at -196°C using a TriStar 3020 (Micromeritics, USA). Sample was pre-treated at 300°C, under vacuum of 50 mTorr, for 1h. The specific surface area was computed from N_2 adsorption isotherms by Brunauer-Emmett-Teller (BET) approach, while the pore size distribution, mean pore diameter and mesopore volume (V_{meso}) were determined by Barrett–Joyner–Halenda (BJH) method, from the desorption branch of the isotherm and assuming the cylindrical pore model.

Atomic force microscopy (AFM) measurements of ferrititanate nanosheets before and after exfoliation were carried out using a Bruker Multimode-8, equipped with JV scanner (125 × 125 × 5 μm). To acquire tapping mode images, an OTESPA probe (spring constant ~42 Nm^{-1}) was employed. Prior to analysis, sample was prepared by drop-casting 20 μL of an aqueous dispersion of pristine and exfoliated ferrititanate nanosheets on a silicon wafer. After drying in air, 2D AFM images were recorded in a low scan rate to perform a quantitative analysis of the thickness distribution of nanosheets using the NanoScope Analysis software (Version 1.5). Thus, several acquired images were selected, all composed of various nanosheets (stacked or individual layers). The software measured the height of each nanosheet at six different points manually selected along a previously specified direction. The same number of measurements has been used for nanosheets before and after delamination.

The UV–Vis absorption spectrum was obtained by diffuse reflectance spectroscopy (DRS) in a Perkin-Elemer Lambda 650 UV/Vis spectrophotometer, using α-Al_2O_3 as a blank reference. The acquired DRS spectrum was plotted as Kubelka-Munk function in order to estimate energy of the bandgap. Raman spectroscopy of exfoliated ferrititanate nanosheets was conducted in a micro-Raman microscope (HORIBA, model XploRA) at the exciting wavelength of 785 nm and using a 50x objective lens. The spectrum was recorded in the range from 50 to 1200 cm^{-1} with a spectral resolution of 4 cm^{-1}.

2.5.2. Characterization of Charge-transfer complex (TiO_2-Acac CT)

N_2 adsorption-desorption, Raman spectroscopy and DRS have been carried out on TiO_2-Acac CT xerogel using the same equipment and conditions as reported in section 2.5.1. X-ray powder diffraction (XRPD) of TiO_2-xerogel/Acac CT was performed in a Bruker D8 Discovery diffractometer, operating with Cu K_α radiation. XRPD patterns were acquired in the range from 10° to 90° 2θ, with a step size of 0.02° (2 s per step). The data analysis was carried using LeBail method with Topas 4.2 software. Particle size distribution of TiO_2-Acac CT was measured by dynamic light scattering (DLS) in a Zetasizer Nano-ZS (Malvern Instruments). The TiO_2-xerogel was also analysed by transmission electron microscopy (TEM) using a JEOL 2010 microscope, operating at 200 kV. For TEM observations, a small amount of TiO_2-xerogel is ultrasonically dispersed in isopropyl alcohol and then dropped onto a holey carbon film supported by a copper grid. Moreover, thermogravimetric analysis (TGA) of charge-transfer complex was carried out in a Perkin-Elmer Simultaneous Thermal Analyzer, STA-6000, in air atmosphere, at a heating rate of 10°C min^{-1} in the temperature range of 30-800°C. Electron paramagnetic resonance (EPR) measurements have been performed either on commercial Miniscope 400 spectrometer (Magnettech-Germany) at room temperature or on home-build EPR spectrometer, at temperatures of 10 K, 30 K and 80 K, using a commercial Bruker X-band resonator coupled to an Oxford He flux cryosystem (ESR 910), Varian magnet and Varian klystron power source. Both spectrometers use 100 kHz field modulation and lock-in detection. Typical parameters were: microwave power 10 mW, sweep time 60 - 300s, central field 300 mT, sweep range 60 - 600 mT, while g factor calibration was done using ZnO:Mn standard. The experiments were performed under UVA (375 nm) illumination.

2.5.3. Characterization of mesoporous nanohybrid heterostructures

The mesoporous nanohybrids were characterized by XRPD, N_2 adsorption-desorption, TGA, TEM and DRS, using the same equipment and similar conditions described in the sections 2.5.1 and 2.5.2. In the case of XRPD, the diffractograms were acquired in the range of 10° to 90° 2θ with a step size of 0.02° (2 s per step) in a D8 Discovery. Fourier-transform infrared spectroscopy (FTIR) of nanohybrids prior and after calcination at 300°C was conducted in a

Scientific Nicolet 670 FTIR spectrometer. Certain amount of each sample was mixed with dried IR-grade KBr and pressed into a pellet, previously to analysis. Spectra were recorded in the range of 1200 to 2300 cm^{-1}, with a resolution of 4 cm^{-1} and 120 scans. Small angle X-ray scattering (SAXS) of nanohybrids was carried out in a Bruker Nanostar SAXS instrument, equipped with Vantec 2000 detector, operating with Cu K_α radiation at 40 kV and 35 mA. The powder sample was placed between two kapton foils. The SAXS data were recorded during 6 h under vacuum and analysed using Sasview software. The sample data were corrected for kapton scattering before analysis.

The heterostructures were also studied by photoluminescence emission spectroscopy (PL) at room temperature using a Spex Fluorolog spectroflurometer with C31034 cooled photomultiplier, under Xenon lamp excitation at 420 nm. The X-ray photoelectron spectroscopy (XPS) was carried out using an Alpha 110 hemispherical analyzer from VG Thermo and the K_α line from Al (1486.6 eV) radiation. The photoelectron spectra associated with the Ti 2p and O 2p core electrons were measured. The C 1s spectrum with the energy of 284.8 eV was used for energy correction. After the correction, the Ti 2p and O 2p peaks were used to determine the oxidation state of Ti and the type of oxygen species presented. Electron Paramagnetic Resonance Spectroscopy (EPR) was performed in the same way as described in details in section 2.5.2.

2.5.4. Measurement of photocatalytic activity

The photocatalytic degradation of NO gas, with the initial content of ~100 ppm of NO, by benchmark P-25 TiO_2, mesoporous nanohybrids (HM-1 and HM-2), TiO_2-xerogel/Acac CT and exfoliated ferrititanate nanosheets was evaluated following the same procedure and equipment described in details by Habran et al., [35]. All tested samples weighted 0.1g. The only modification was that three T5 tubular fluorescent lamps (visible light) of 8 W (λ= 400 – 700 nm) have been used, instead of UVA lamps, while the irradiance of light source was 0.77 Wcm^{-2}. The photocatalytic degradation of NO was monitored as the percentage of conversion of NO molecules during a time interval of 120 min. Therefore, the photocatalytic activity of each sample was estimated through the integrated area below the NO conversion (%) *vs*. time curve [35]. The deactivation mechanism, observed through the reduction of photocatalytic activity with time, is due to

adsorption of mineralized NO_3^- species, during photo-oxidation of NO, on the semiconductors surface and will be reported in detail elsewhere.

3. RESULTS

3.1. Exfoliated ferrititanate nanosheets

Protonated ferrititanate nanosheets exfoliated by the mechanochemical procedure, described in the section 2.2, were examined in details in a previous report [26]. Almost total exfoliation of these nanosheets was suggested by XRPD and TEM analyses and corroborated by SAXS measurements [34].

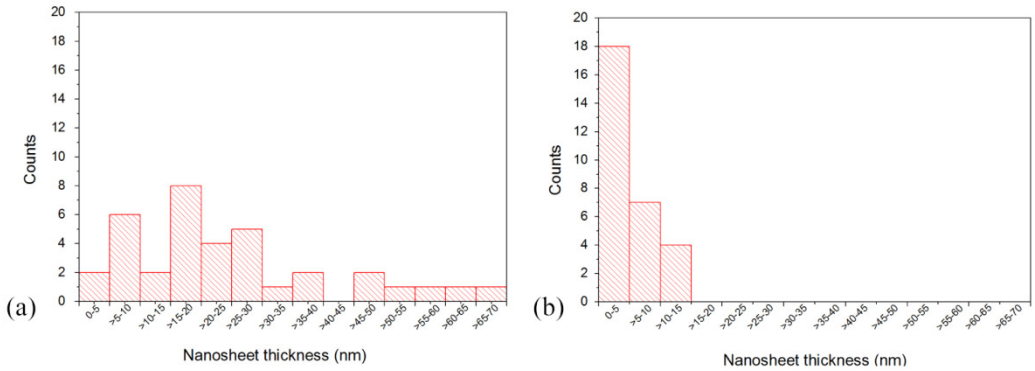

Figure 2. Thickness distribution histograms of protonated ferrititanate nanosheets (a) before (p-NS) and (b) after exfoliation with TBAOH molecules (p-NS/TBA^+).

Table 1. Specific surface area (S_{BET}), mesopore volume (V_{meso}) and mean pore diameter of exfoliated ferrititanate nanosheets (p-NS/TBA^+), TiO_2-xerogel and nanohybrids HM-1 and HM-2.

	p-NS/TBA^+	TiO_2-Acac CT	HM-1	HM-2
S_{BET}, m^2g^{-1}	60	132	139	153
***V_{meso} (BJH),* mLg^{-1}**	0.184	0.072	0.166	0.223
***Mean pore diameter (BJH),* nm**	16.5	2.9	5.0	5.1

N_2 adsorption-desorption, Raman spectroscopy and quantitative AFM analyses have been carried out to better comprehend the final product of the exfoliation procedure. Quantitative AFM analyses (Figure 2a,b) demonstrated that before exfoliation procedure, the thickness of nanosheets varied in a broad range, starting from few nanometers until 70 nm, while after exfoliation most of the nanosheets present a thickness smaller than 5 nm, among which prevail those with the thickness of ~1-2 nm, corresponding to exfoliated single, or double, host layers, considering the thickness of a single host ferrititanate layer around 1 nm [26] (Supplementary Material s6, figure s2). The as-exfoliated nanosheets possess

a specific surface area of 60 m^2g^{-1} and relatively large mesopores (Table 1 and Fig. 3b). The isotherm of exfoliated ferrititanate nanosheets (Figure 3) can be classified as type IV, a characteristic of mesoporous adsorbents. The hysteresis loop can be classified as H3, in accordance to IUPAC classification, a fingerprint of lamellar particles that form slit-shaped pores.

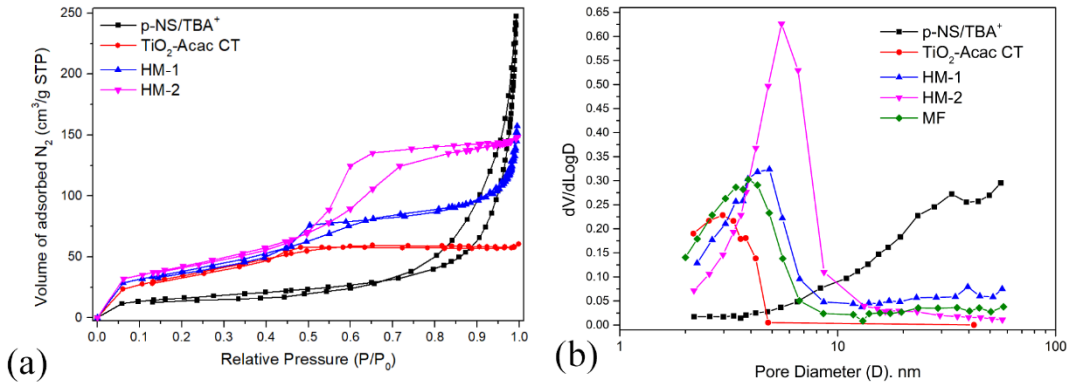

Figure 3. (a) N_2 adsorption-desorption isotherms of exfoliated ferrititanate nanosheets (p-NS/TBA^+), TiO_2-xerogel (TiO_2-Acac CT), and nanohybrids (HM-1 and HM-2); and (b) BJH plots of the differential pore volume (dV/dlogD) as a function of pore diameter (D).

Raman spectrum (Figure 4) shows bands at the wavenumbers ≥ 200 cm^{-1} that may correspond to Ti-O vibrations within the lepidocrocite layer [53]. Gao et al. [53] reported an exhaustive Raman Spectroscopy characterization of different Lepidocrocite-type layered structures. Nine Raman lines ($3A_g$ +$3B_{1g}$+ $3B_{3g}$) corresponding to Raman-active modes expected from this orthorhombic structure (space group Immm) are recorded at 183, 270, 387, 449, 558, 658, 704, 803, and 908 cm_{-1}, and assigned to Ti-O lattice vibrations within the two-dimensional lepidocrocite-type TiO_6 octahedral layers. These diagnostic Raman bands present a clear signature for a protonic titanate lepidocrocite-type layered structure. However, depending on the molecules intercalated between the titanate nanosheets these nine active Raman band can shift, or can present variation in the intensity. Nine Raman bands of dehydrated titanate nanosheets are recorded at 181, 282, 389, 447, 560, 657, 708, 816 and 930 cm^{-1} [53]. Finally, eleven Raman bands of TBA-intercalated titanate nanosheets are recorded at 181, 275, 383, 444, 558, 656, 701, 793, 828, 882 and 914 cm^{-1} [53]. The Raman spectrum of exfoliated TBA-ferrititanate nanosheets (Figura 4) presented the following 12 vibration transitions: 144, 202, 281, 355, 404, 542, 664, 697, 781, 880, 911 and 951 cm^{-1}. The origin of the Raman band at 144 cm^{-1}, has been explained, in more details in the following paragraph, by the presence of trititanate nanosheet [55].

The rest of eleven bands correspond to the Ti-O vibration of TiO_6 octahedrons and interlayer TBA molecules (880 and 951 cm^{-1}). We also consider, that the presence of Fe ions can break the symmetry of the orthorhombic structures, which allows the shift of vibration transitions and variation of their relative intensities [53].

However, a strong band at around 144 cm^{-1} is also present. Peak et al., [54] observed the same band splitting in their nanotitanates, obtained after alkaline hydrothermal treatment of protonated lepidocrocite-like titanates, and attributed this feature to the layered trititanate crystal structure, a structure related to the lepidocrocite one. The same Raman band splitting and formation of a band at ~144 cm^{-1}, due to trititanate crystallization, were found, as well, by Horvath et al. [55]. Thus, trititanate nanosheets may also be present in the exfoliated material in some extent, together with the predominant lepidocrocite-like titanate. These two layered nanostructures may have co-precipitated during the alkaline hydrothermal stage.

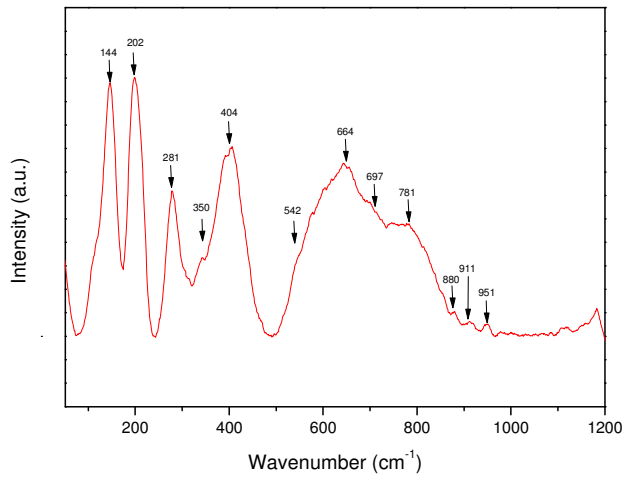

Figure 4. Raman spectrum of exfoliated ferrititanate nanosheets.

3.2. Charge-transfer complex (TiO_2-Acac CT)

The sol-gel route led to very small and uniform anatase nanocrystals associated with Acac, thereby forming a CT complex. XRPD pattern of the xerogel was adjusted by the LeBail method and mean crystallite size as small as 2.5 nm was estimated (Figure 5a). The same analysis suggested that ~20% of the titania was still amorphous. Dynamic light scattering measurements resulted in a mean particle size of ~4 nm (Figure 5b), which was corroborated by TEM image analysis (Figure 5c). Raman spectrum (Figures 5d) of the anatase-xerogel showed

a band (E_g) at around 145 cm^{-1}, broader than the same band acquired for the commercial TiO_2 nanopowder P-25 (Evonik) [8], which is another indication of very small crystallite sizes. A small shift (~10 cm^{-1}) of the Ti-O vibration band in TiO_2-Acac CT might be due to the presence of amorphous content as detected by XRPD.

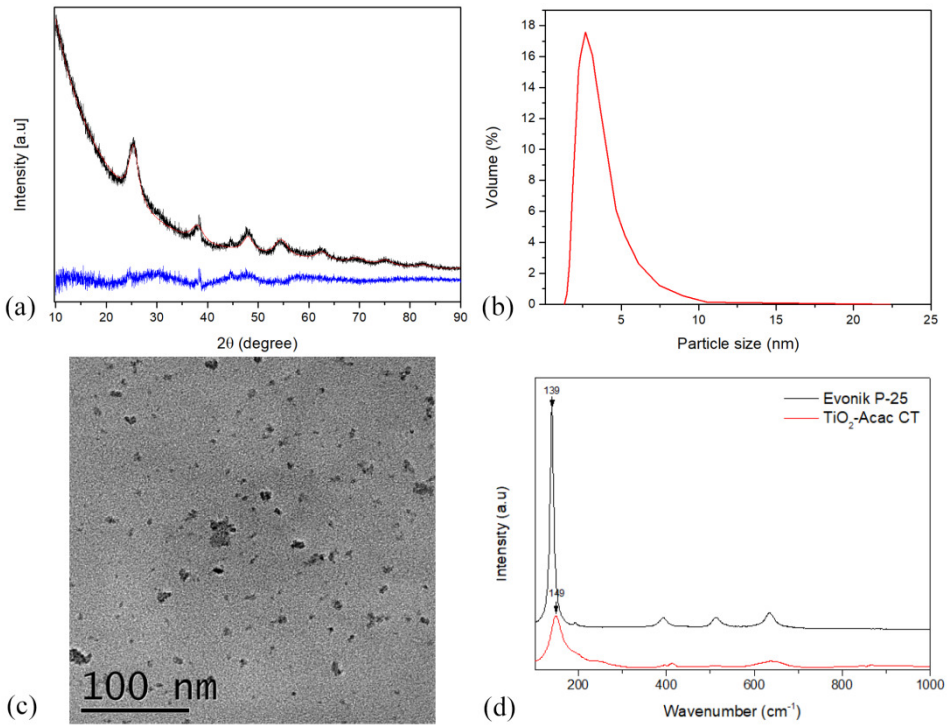

Figure 5. (a) XRPD pattern of TiO_2-xerogel, illustrating the LeBail fit to anatase space group I $4_1/a$ m d (the experimental pattern is black, the calculated pattern is red and the difference plot is blue; b) Particle size distribution of TiO_2-xerogel measured by DLS; (c) TEM image of TiO_2-xerogel and (d) Raman spectra of TiO_2-xerogel (TiO_2-Acac CT) and TiO_2 powder (Evonik P-25).

From TGA analysis (Figure 6) a total mass loss of 25 wt% was observed along three stages. The first one, represented by the peak at temperature lower than 100°C in the derivative thermogravimetry curve (DTG), is mainly due to moisture release. The second and the third stages, with the peaks at 240°C and 345°C, are ascribed to volatilization of acetylacetonate [51]. The major mass loss, >10%, occurred along the third stage at temperatures superior to 300°C, due to the loss of acetylacetonate.

N_2 adsorption-desorption curve of TiO_2-Acac CT (Figure 3) is of type I, ascribed to microporous adsorbents, while the measured specific surface area is 132 m^2g^{-1}. This value is in accordance with some previous reports on textural properties of TiO_2 synthesized through sol-gel route [48,56].

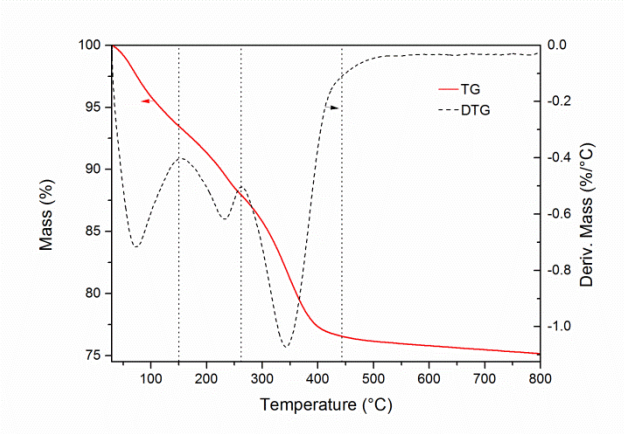

Figure 6. TGA and DTG curves of TiO_2-xerogel.

The red-yellowish color of the TiO_2-xerogel (Figure 7a) is an indication of the extension in absorption range from UV to the higher-energy part of visible spectrum. The Kubelka-Munk plot (Figure 7b), obtained from DRS spectrum, confirms the formation of the TiO_2-Acac CT with the band-gap of 2.5 eV, in comparison to pure titania P-25 with the band-gap of 3.2 eV. The origins of the CT phenomenon have been proposed and thoroughly discussed recently by Sannino et al., [48] who pointed out to the direct injection of excited electrons from the HOMO of Acac into the CB of anatase as the mechanism responsible for the extension of absorption of anatase into visible region. No HOMO to LUMO (lowest-unoccupied-molecular-orbitals) transition is possible to occur within the visible light spectrum due to a large energy gap (> 3.2 eV) between those two molecular orbitals inside Acac electronic structure.

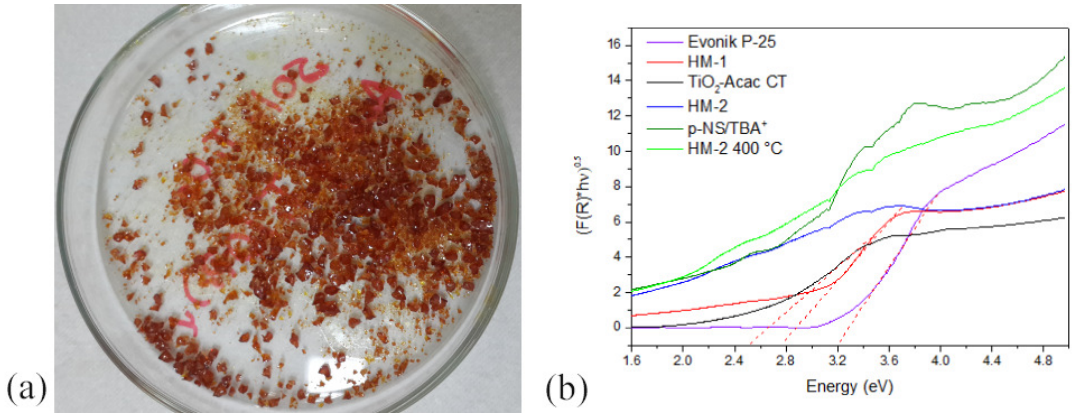

Figure 7. (a) TiO_2-xerogel (TiO_2-Acac CT) and (b) Kubelka-Munk plots obtained from DRS spectra of exfoliated ferrititanate (p-NS/TBA^+), TiO_2-xerogel (TiO_2-Acac CT), nanohybrids (HM-1 and HM-2), and Evonik P-25 TiO_2.

EPR spectra, acquired at 10, 30 and 80K, (Supplementary Material S7, figure s3) revealed the presence of $O_2^{\bullet-}$, a ROS necessary for the oxidation of NO into NO_3^-, as well as of two types of point defects inside anatase structure, self-trapped electron oxygen vacancy (SETOV) and Ti^{3+}.

3.3. Mesoporous nanohybrids

The preparation of the mesoporous nanohybrid is a two-stage process consisting of a soft-chemical part and of a posterior calcination at a relatively low temperature. While the former stage is carried out to mix together the two components and to achieve a high number of heterojunctions between the two semiconductors, the other is performed with the goal to assure better electrical contacts, however, with minimum particle growth, and to promote crystallization of the non-crystalline part of titania (Fig. 5a). Since the anatase is linked to Acac, forming a CT, calcination temperature must not exceed the temperature of complete volatilization of Acac (~ 400°C, Fig. 6). TG curves of these mesoporous materials before calcination (denoted as PC) are depicted in Figure 8a. The weight loss until 130°C is due to the release of physically adsorbed water (and ethanol, in the case of HM-2). Since HM-2 material is prepared from TiO_2-sol the weight loss up to 130°C is much higher than that in the case of HM-1, where TiO_2-xerogel was used, after oven drying at 100°C. The weight loss, before calcination (Figure 8a), at the temperatures between 130°C and 400°C, attributed mainly to the Acac release, is almost the same (4.8 and 4.6 wt.%) for HM-1 and HM-2, respectively. TG curves of the nanohybrids calcined at 300°C are presented in Figure 8b. The weight loss between 130 and 400°C, assigned to the release of Acac, is also similar for both nanohybrids calcined at 300°C and varies between 2.1 and 3.3 wt.% for HM-1 and HM-2, respectively. In contrast, the TG curve of the nanohybrid (HM-2) calcined at 400°C showed an insignificant weight loss in this temperature range (0.7 wt.%) and confirmed that Acac is almost completely removed after calcination at 400°C, in accordance to TGA curve (Figure 6).

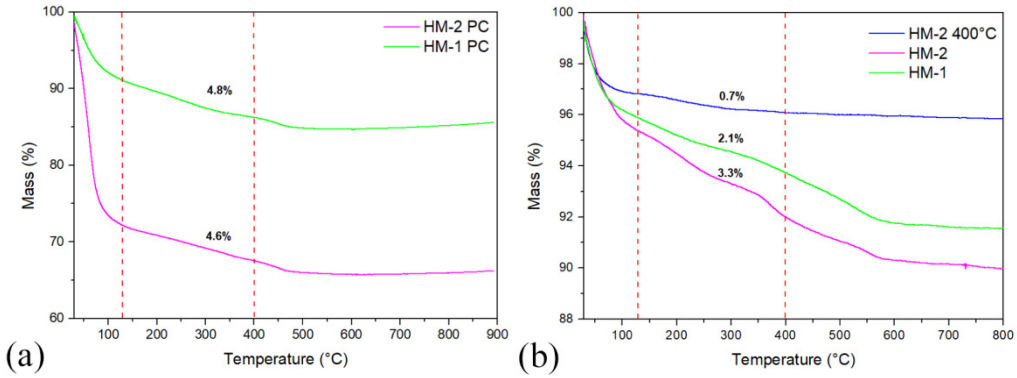

Figure 8. TGA curves of nanohybrids (HM-1 and HM-2) (a) before and (b) after calcination at 300 °C. In the case of HM-2 nanohybrid, the calcination was also performed at 400 °C.

The FTIR spectra of heterostructures before calcination (Supplementary Material s8, figure s4) showed an absorption band at 1380 cm^{-1} due to ν(CO) vibration, attributed to Acac [57]. The band is faint for the calcined materials (Supplementary Material s8, figure s4), although still present, confirming, therefore, the maintenance of Acac in the nanohybrids, after calcination at 300°C.

XRPD patterns of the two nanohybrids presented similar features (Figure 9a). All patterns showed the (101) diffraction line of anatase phase situated at ~25.1° (2θ), together with a low intensity anatase line at higher 2θ angles (~38°) and faint diffraction lines from hematite at 33.2 and 35.7 (2θ) [25]. There was no evidence of pillarization at lower interlayer distances. The appearance of anatase diffraction lines evidenced that, at least, some anatase is not intercalated within ferrititanates single layers. On the other hand, SAXS patterns resulted rather different (Figure 9b). SAXS pattern of HM-1showed a strong broad peak, centered at 9.7 nm, which suggests that restacking occurred, only partially however, since a part of the anatase was identified by XRPD as independent phase by 25.1° (2θ) line (Figure 9a). An average interlayer distance of 9.7 nm is compatible with the pillars composed of two interlayeres of TiO_2 particles with the mean size of ~4 nm (Figure 5b) and the exfoliated single host ferrititanate layer with the thickness of ~1 nm [26]. HM-2 presented a weaker peak in comparison to HM-1, centered at ~9.0 nm, also understood as an indication of partial pillaring inside HM-2 nanohybrid. In both cases, the good dispersion of TiO_2-Acac nanoparticles and titanate nanosheets in aqueous medium can lead to their close interaction, which may explain the indication of some pillaring. Their

mutual organization as a non-pillared “house-of-card” arrangement [58] is also a possibility and would explain the certain extent of TiO_2 preserved as an independent XRPD phase.

HM-1, HM-2 and HM-1 400°C heterostructures have been thoroughly studied by TEM. One of the principal observations regards to the similar size of anatase nanoparticles inside HM-2 and HM-2 400°C heterostructures (Supplementary Material s9, figure s5), meaning that no significant particle growth occurred in the heterostructures calcined at 300°C and 400°C. The heterostructures HM-1 and HM-2 generally consist of well mixed components, i.e., nanoparticles supported over exfoliated nanosheets (figure s5). At higher magnifications it is possible to observe the typical morphology of a nanosheet [24,26], supporting anatase nanoparticles, (Supplementary Material s10, figure s6).

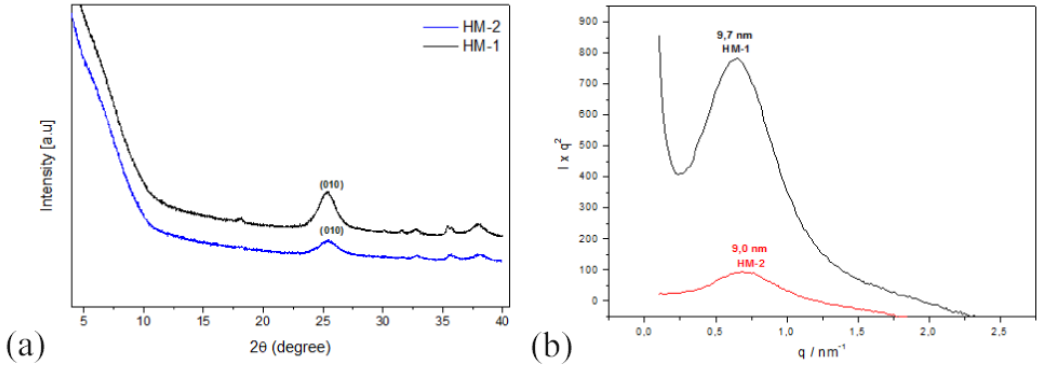

Figure 9. (a) XRPD and (b) SAXS patterns of HM-1 and HM-2 nanohybrids.

N_2 adsorption-desorption isotherms, pore distribution curves and the values of textural properties of HM-1and HM-2 are presented in Figure 3 and Table 1. HM-1 exhibited a N_2 adsorption-desorption isotherm with mixed features of the types II and IV, while HM-2 showed a pure Type IV isotherm with the hysteresis loop H4 according to IUPAC classes, typical of catalytic mesoporous solids. HM-2 showed a slightly higher specific surface area (153 *vs.* 139 m^2g^{-1}), but both values were superior to that of its separated components. HM-2 and HM-1showed similar mean pore size of ~ 5 nm, but HM-2 contained significantly higher mesopore volume (see Fig. 3-b).

The Kubelka-Munk plots are displayed in Figure 7b. HM-1 demonstrated the characteristic bandgap of 2.8 eV, a feature of TiO_2-Acac CT, however, absorption tail continues significantly in the whole visible spectrum, while for the

pure TiO_2-Acac CT component it decreases more rapidly after 2.5 eV. It is, therefore, evident the combined optical features of the two semiconducting components. By comparison, Kubelka-Munk plot of HM-2 showed absorption over the entire UV-visible spectrum with no clear inflexion point, thus making it difficult to ascribe a value for the band-gap of HM-2. A similar feature is noticed for HM-2 400°C.

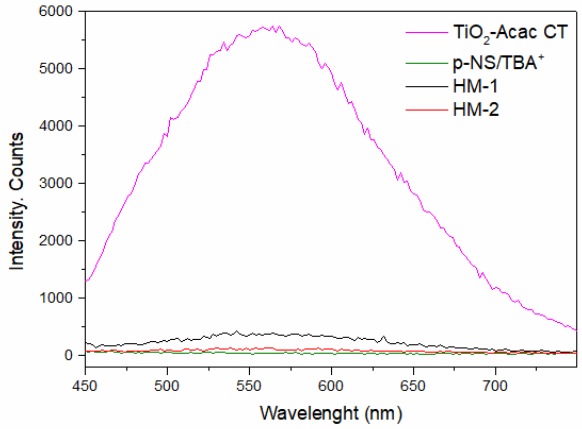

Figure 90. PL spectra of nanohybrids (HM-1 and HM-2), TiO_2-xerogel (TiO_2-Acac CT) and exfoliated ferritanate nanosheets (p-NS/TBA^+).

The PL spectra of mesoporous nanohybrids and their individual components, excited by the wavelength of 420 nm, are shown in Figure 10. TiO_2-Acac CT presented a strong emission signal, centred at ~550 nm (~2.25 eV), due to the recombination of excited electrons from anatase CB to the HOMO of Acac molecules, with consequent photon emission. On the other hand, the quenching process is verified for both mesoporous nanohybrids. The quenching process is only possible if a charge separation mechanism is active. Considering the relationship between the electronic band structures of the two involved semiconductors [27,48], exfoliated lepidocrocite-like ferrititanates and TiO_2-Acac CT, quenching can be understood through the electron injection from anatase CB into the unoccupied Fe^{3+} 3*d* states (E_g), serving as trapping sites within the band-gap of exfoliated ferrititanate. A possible scheme of electronic bands for the ferrititanate-TiO_2-Acac CT heterojunction and the charge separation mechanism is depicted in Figure 11. A similar mechanism of charge separation has been suggested by Zhang et al [59] for the case of straddled TiO_2/Fe_2O_3 heterojunction, where anatase crystals presented electron trapping sites below Fe_2O_3

CB, at a level ~ 0.8 eV lower than the bottom of anatase CB [60]. Considering EPR spectrum of TiO_2-Acac (item 3.2) it is possible that some free electrons from anatase CB have been trapped also in SETOV and Ti^{3+}. However, the presence of these species in mesoporous nanohybrids could not be confirmed by EPR of heterostructures due to an intense peak dominating the spectra, especially at higher temperatures, probably of ferri- or ferromagnetic origin, while at lower temperature the structural Fe^{3+} peak prevails (Supplementary Material s7, figure s3).

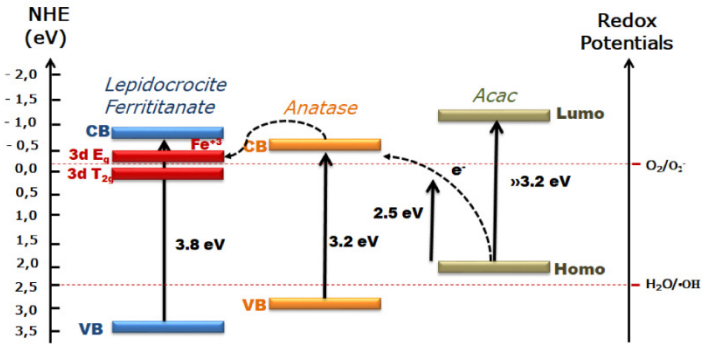

Figure 101. Scheme of electronic bands for the ferrititanate-CT heterojunction and the proposed charge separation path.

3.4. Photocatalytic degradation of NO gas under visible light

Photocatalytic tests for NO degradation, as summarized in Figure 12a,b, pointed out to the highest activity of HM-1, 4 times higher in comparison to P-25, which has relativly low activity in visible spectrum as expected, considering the band gaps of its constituent semiconductors, anatase and rutile. HM-1 exhibited higher conversion of NO than their separate components (ferrititanate and TiO_2-Acac CT), thus demonstrating a synergetic effect for photocatalytic degradation of NO.

TiO_2-Acac CT is 2.5 times more active than P-25, while HM-2 showed activity nearly comparable to P-25. It is worth noting that HM-2 400°C is inactive even in comparison to HM-2 and P-25, as the consequence of Acac loss, thus lacking the principal visible light absorption mechanism. Exfoliated ferrititanates can be considered inactive regarding to NO degradation, although exhibits a massive absorption within visible light spectrum.

It is worth noting that the toxic intermediate oxidation product NO_2 was not detected for the tested materials, indicating that the photooxidation proceeded to its final stage, resulting in the formation of NO_3^- species.

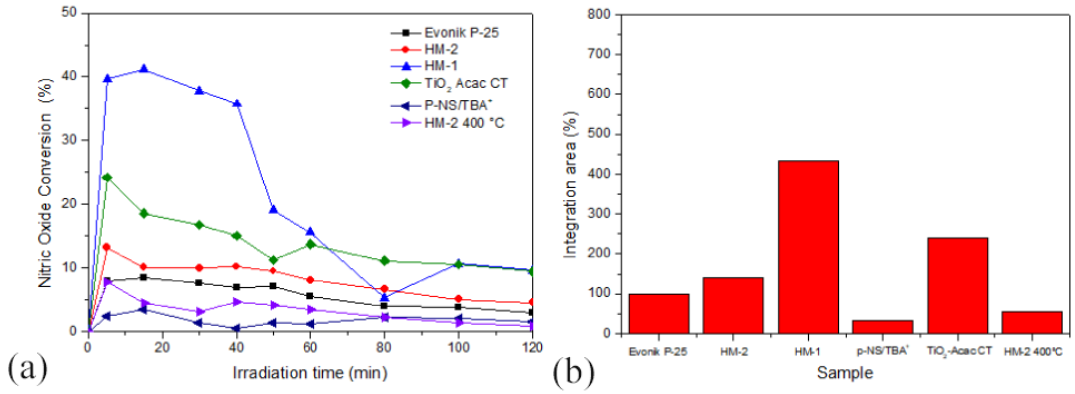

Figure 12. (a) Photocatalytic conversion of NO as a function of time for Evonik P-25 TiO_2, nanohybrids (HM-1 and HM-2) and semiconducting components (TiO_2-Acac CT, p-NS/TBA^+), and (b) histograms of photocatalytic activity obtained through integration area approach.

4. Discussion

The absorption mechanism under visible light and charge separation of the as-prepared heterojunctions, as proposed and depicted in Figure 11, first deserves to be discussed in more details.

Visible light absorption paths. Under visible light irradiation free electron-to-hole pairs cannot be formed in anatase or ferrititanate through the excitation of electrons from their valance band (VB) to CB, since in both cases more energetic UV light is needed. Therefore, visible light is absorbed in two possible ways within the heterojunctions HM-1 and HM-2. One is, as previously proposed, the injection of electrons from HOMO of Acac into anatase CB. The second mode is restricted to ferrititanate and might consist of the transfer of electrons between Fe^{3+} *d*-levels ($T_{2g} \rightarrow E_g$) or from VB to empty Fe^{3+} state (E_g), while transfer from full Fe^{3+} d-state (T_{2g}) to ferrititanate CB [61] may also contribute. Free electrons injected into ferrititanate CB may decay to the anatase CB with higher redox potential [27], from where these can take part in the reduction reaction of O_2 or recombine to iron *d*-levels ($Fe^{4+} + e^-_{CB} = Fe^{3+}$).

Charge separation paths. Considering high [Ti] anatase/[Ti] ferrititanate mol ratio, the charge separation occurs, predominantly, by electron decaying from anatase CB into Fe^{3+} trapping site through the following reaction: $Fe^{3+} + e^-_{CB}(TiO_2) \Rightarrow Fe^{2+}$. The processes of electron injection into anatase CB from HOMO of Acac and, afterwards, to iron trapping sites inside ferrititanates lead to a robust charge separation, suggesting that the reduction reaction $O_2 + e^-_{CB} \Rightarrow O_2^{\bullet-}$ may occur on anatase CB, as well as on the Fe^{3+} trapping sites inside

ferrititanates. The second reaction (the oxidation one), $OH^- + h^+_{VB} \Rightarrow OH^\bullet$ may proceed on VB of ferrititanate capable to oxidize H_2O/OH^-.

It is worth noting that both mesoporous nanohybrids exhibit quenching of fluorescence emission (Figure 10). Therefore, the previously proposed mechanism of charge separation operates in HM-1 and HM-2. The most intense quenching occurs for HM-2 heterojunction, suggesting that this material presents the highest number of well-formed electrical junctions between the two semiconductor components. Indeed, HM-2 was prepared from TiO_2 sol and a more intimate contact between the semiconducting components in this nanohybrid material as compared to HM-1would be a reasonable assumption. The question is why this apparent advantage has not been converted into a better photocatalytic activity for HM-2 (item 3.4 – Fig. 12).

An insight in such a behavior can be undertaken through Urbach energy analysis of the data collected by DRS [28,62]. Urbach energy is related to the absorption tail that may appear in Kubelka-Munk plot over the energy range lower than the band gap energy. It is directly related to the amount of defect states inside band gap and, therefore, to sub-band gap transitions. It is calculated by linearizing the following empirical equation:

$$\alpha^* = \alpha_o exp((h\nu - E_o)/E_u)$$

where α^* is the absorption coefficient, α_o, E_o are the materials properties and E_u is the Urbach energy (obtained from the reciprocal slope value of the linearized equation). Such analysis has been performed for the two heterostructures (Figure 13). Urbach energy for HM-2 is much higher than that of HM-1, 900 and 270 meV, respectively. It is also worth noting that E_u for HM-2 is much higher than the values commonly observed for semiconductors such as TiO_2 and SnO_2 [28,62–64]. This is a sign of a high number of defects inside HM-2, which can act as recombination centers and cause reduction of photocatalytic activity [63]. Therefore, charge separation in HM-2 is likely impaired by recombination process into defects with energy levels within ferrititanate or anatase bandgaps. It is known that different preparation routes of a photocatalyst can lead to very different concentaration of defects and, consenquently, to significant increase of Urbach energy if this concentration is high [62]. Since TiO_2-sol is used for the

preparation of HM-2 heterostructure, insead of TiO_2-xerogel, it can be rationalized that the as-prepared heterojunction still contains an anatase with high concentartion of defects deep inside bandgap which serve as recommbination sites and do not contribute to the reduction reaction and the formation of $O_2^{\bullet-}$ ROS.

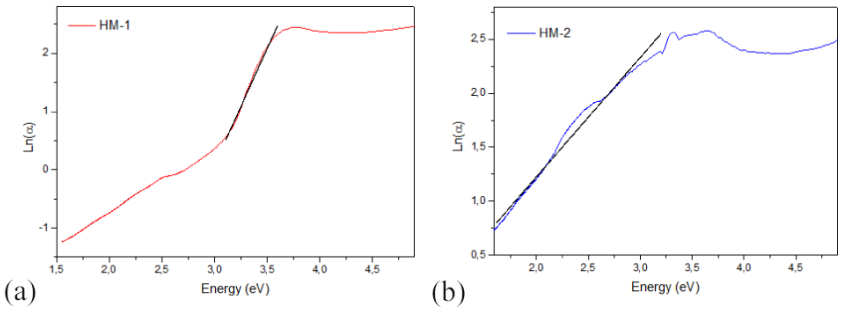

Figure 113. Urbach energy graphs obtained from Kubelka-Munk plots of the mesoporous nanohybrids (a) HM-1, (b) HM-2.

A successful charge separation is, however, just one of the several fundamental stages responsible for the achievement of high photocatalytic efficiency. After charge separation is successfully accomplished, two posterior stages, **a)** ROS ($OH^{\bullet}$ and $O_2^{\bullet-}$) formation and **b)** ROS induced oxidation of NO molecules, have to be efficiently accomplished in order to impart high photocatalytic activity. It has already been stressed in literature that a higher content of adsorbed O_2 or H_2O/OH^- species enhances photocatalytic activity of TiO_2 [65,66]. However, XPS analysis (Figure 14) revealed that the two nanohybrids, besides the lattice oxygen with the peak centred at ~530 eV, present almost the same quantities of the oxygen from hydroxide ions, identified through the peak situated at the energies higher than 530 eV, but lower than 532.5 eV [66,67]. Titanium cations appear in both nanohybrids, exclusively, as Ti^{4+}, i.e., no sign of Ti^{3+} (Supplementary Material s11 figure s7). This observation is not in conflict with EPR observation of Ti^{3+}, since EPR data have been collected under UV illumination.

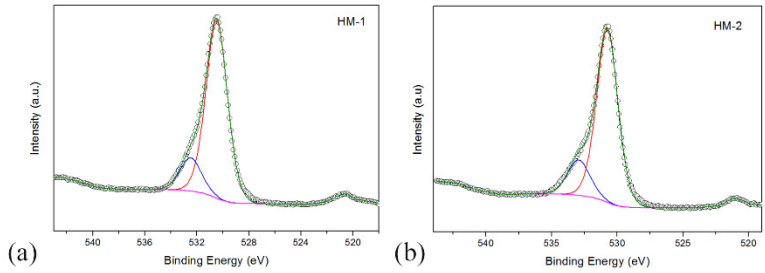

Figure 124. XPS spectra of mesoporous nanohybrids (a) HM-1, and (b) HM-2.

[Ti] anatase/[Ti] ferrititanate mol ratio might also play a role in photocatalytic efficiency. Although, the nominal ratio of 20 was designed for the synthesis of both HM-1and HM-2, they experimentally resulted in the ratios of 19 and 26, respectively. The lower ratio of HM-1 may have been, at least partly responsible, for the synergetic effect of the two semiconductor components (Figure 12). This occurrence put in evidence the effect of the amount of exfoliated ferrititanate inside the heterostructure on its photocatalytic efficiency inasmuch as the photocatalytic activity increased with the increased proportion of layered ferrititanate; of course, this might be valid for the short range of [Ti] anatase/[Ti] ferrititanate mol ratios studied herewith between 19 and 26.

5. Conclusions

New mesoporous heterostructures, sensitive to visible light and exhibiting an efficient charge separation mechanism, has been successfully synthesized starting from exfoliated ferrititanates with lepidocrocite structure and a charge transfer complex, consisted of TiO_2 (anatase) and acetylacetonate.

Visible light sensitivity is reached in two ways, through direct injection of electrons into anatase CB from acetylacetonate HOMO and by absorption of ferrititanate, which presents fully occupied T_{2g} states of Fe^{3+} localized above VB of lepidocrocite ferrititanate and unoccupied E_g states situated below CB. Charge separation mechanism is based primarily on free electron transition from anatase CB into Fe^{3+} trapping site within ferrititanate band-gap.

Photocatalytic degradation of NO under visible light irradiation showed considerable efficiency for the heterostructure denoted HM-1 in comparison to the benchmark photocatalytic material TiO_2-P25. Heterostructure denoted HM-2 showed lower photocatalytic degradation efficiency, which is tentatively ascribed to the high number of defect sites, possibly, with the bang-gaps of ferrititante and anatase, as observed from its high Urbach energy.

A synergetic effect between the two semiconducting components, only achieved in the HM-1 heterostructure, may also be also related to its somewhat lower [Ti] anatase/[Ti] ferrititanate mol ratio, indicating the importance of the fine control of the proportion of these components inside the heterostructure for the best photocatalytic degradation efficiency. However, the effect of [Ti] anatase/[Ti] ferrititanate mol ratio on photocatalytic properties should be studied in a more systematic manner in order to elucidate its real impact.

Acknowledgments

B.A.M. is grateful to CNPq (National Council for Scientific and Technological Development) for a Research Productivity Grant. M.H is grateful to CNPq for scholarship. O.P. is grateful to CNPq for financial support.

References

[1] J. Schneider, M. Matsuoka, M. Takeuchi, J. Zhang, Y. Horiuchi, M. Anpo, D.W. Bahnemann, Understanding TiO_2 Photocatalysis: Mechanisms and Materials, Chem. Rev. 114 (2014) 9919–9986.

[2] L. Sang, Y. Zhao, C. Burda, TiO_2 Nanoparticles as Functional Building Blocks, Chem. Rev. 114 (2014) 9283–9318.

[3] S. Banerjee, J. Gopal, P. Muraleedharan, a K. Tyagi, B. Raj, Physics and chemistry of photocatalytic titanium dioxide : Visualization of bactericidal activity using atomic force microscopy, Curr. Sciense. 90 (2006) 1378–1383.

[4] B. Kraeutler, A.J. Bard, Heterogeneous photocatalytic decomposition of saturated carboxylic acids on titanium dioxide powder. Decarboxylative route to alkanes, J. Am. Chem. Soc. 100 (1978) 5985–5992.

[5] L. Spanhel, H. Weller, A. Henglein, Photochemistry of semiconductor colloids. 22. Electron ejection from illuminated cadmium sulfide into attached titanium and zinc oxide particles, J. Am. Chem. Soc. 109 (1987) 6632–6635.

[6] K.R. Gopidas, M. Bohorquez, P. V. Kamat, Photophysical and photochemical aspects of coupled semiconductors: charge-transfer processes in colloidal cadmium sulfide-titania and cadmium sulfide-silver(I) iodide systems, J. Phys. Chem. 94 (1990) 6435–6440.

[7] N. Serpone, E. Borgarello, M. Grätzel, Visible light induced generation of hydrogen from H_2S in mixed semiconductor dispersions; improved efficiency through inter-particle electron transfer, J. Chem. Soc., Chem. Commun. (1984) 342–344.

[8] B. Ohtani, O.O. Prieto-Mahaney, D. Li, R. Abe, What is Degussa (Evonik) P25? Crystalline composition analysis, reconstruction from isolated pure particles and photocatalytic activity test, J. Photochem. Photobiol. A Chem. 216 (2010) 179–182.

[9] D.O. Scanlon, C.W. Dunnill, J. Buckeridge, S.A. Shevlin, A.J. Logsdail, S.M. Woodley, C.R.A. Catlow, M.J. Powell, R.G. Palgrave, I.P. Parkin, G.W. Watson, T.W. Keal, P. Sherwood, A. Walsh, A.A. Sokol, Band alignment of rutile and anatase TiO_2, Nat. Mater. 12 (2013) 798–801.

[10] T. Sato, K. Masaki, T. Yoshioka, A. Okuwaki, Photocatalytic properties of CdS and CdS-ZnS mixtures incorporated into the interlayer of layered compounds, J. Chem. Technol. Biotechnol. 58 (2007) 315–319.

[11] J. Choy, H. Lee, H. Jung, H. Kim, H. Boo, Exfoliation and restacking route to anatase-layered titanate nanohybrid with enhanced photocatalytic activity, Chem. Mater. (2002) 2486–2491.

[12] J.-H. Choy, H.-C. Lee, H. Jung, S.-J. Hwang, A novel synthetic route to TiO_2-pillared layered titanate with enhanced photocatalytic activity, J. Mater. Chem. 11 (2001) 2232–2234.

[13] Y. Fujishiro, S. Uchida, T. Sato, Synthesis and photochemical properties of semiconductor pillared layered compounds, Int. J. Inorg. Mater. 1 (1999) 67–72.

[14] S.M. Paek, H. Jung, Y.J. Lee, M. Park, S.J. Hwang, J.H. Choy, Exfoliation and reassembling route to mesoporous titania nanohybrids, Chem. Mater. 18 (2006) 1134–1140.

[15] B. Wang, Y. Bai, Z. Xing, D. Hulicova-Jurcakova, L. Wang, Enhanced Performance of a Pillared TiO_2 Nanohybrid as an Anode Material for Fast and Reversible Lithium Storage, ChemNanoMat. 1 (2015) 96–101.

[16] Z.J. Chen, B.Z. Lin, B.H. Xu, X.L. Li, Q.Q. Wang, K.Z. Zhang, M.C. Zhu, Preparation and characterization of mesoporous TiO_2-pillared titanate

photocatalyst, J. Porous Mater. 18 (2011) 185–193.

[17] J. Yang, J. Ding, Preparation and characterization of alumina-pillared ultrafine layered tetratitanate, Mater. Lett. 58 (2004) 3872–3875.

[18] M. Yanagisawa, S. Uchida, Y. Fujishiro, T. Sato, Synthesis and photocatalytic properties of titania pillared $H_4Nb_6O_{17}$ using titanyl acylate precursor, J. Mater. Chem. 8 (1998) 2835–2838.

[19] J.-H. Yang, H. Piao, A. Vinu, A.A. Elzatahry, S.-M. Paek, J.-H. Choy, TiO_2-pillared clays with well-ordered porous structure and excellent photocatalytic activity, RSC Adv. 5 (2015) 8210–8215.

[20] B.Z. Lin, X.L. Li, B.H. Xu, Y.L. Chen, B.F. Gao, X.R. Fan, Improved photocatalytic activity of anatase TiO_2-pillared $HTaWO_6$ for degradation of methylene blue, Microporous Mesoporous Mater. 155 (2012) 16–23.

[21] T.W. Kim, S.G. Hur, S.-J. Hwang, H. Park, W. Choi, J.-H. Choy, Heterostructured Visible-Light-Active Photocatalyst of Chromia-Nanoparticle-Layered Titanate, Adv. Funct. Mater. 17 (2007) 307–314.

[22] S. Pavasupree, Y. Suzuki, S. Yoshikawa, R. Kawahata, Synthesis of titanate, TiO_2 (B), and anatase TiO_2 nanofibers from natural rutile sand, J. Solid State Chem. 178 (2005) 3110–3116.

[23] L.T. Mancic, B.A. Marinkovic, P.M. Jardim, O.B. Milosevic, F. Rizzo, Precursor Particle Size as the Key Parameter for Isothermal Tuning of Morphology from Nanofibers to Nanotubes in the $Na_{2-x}H_xTi_nO_{2n+1}$ System through Hydrothermal Alkali Treatment of Rutile Mineral Sand, Cryst. Growth Des. 9 (2009) 2152–2158.

[24] P.M. Jardim, L. Mancic, B. a. Marinkovic, O. Milosevic, F. Rizzo, $Na_{x-y}H_yTi_{2-x}Fe_xO_4 \cdot nH_2O$ nanosheets with lepidocrocite-like layered structure synthesized by hydrothermal treatment of ilmenite sand, Cent. Eur. J. Chem. 9 (2011) 415–421.

[25] A.M.L.M. Costa, B.A. Marinkovic, N.M. Suguihiro, D.J. Smith, M.E.H.M. da Costa, S. Paciornik, Fe-doped nanostructured titanates synthesized in a single step route, Mater. Charact. 99 (2015) 150–159.

[26] B.A. Marinkovic, P.I. Pontón, J.M. Resende, S. Letichevsky, M. Habran, J.B.

Viol, O. Pandoli, L. Mancic, Lepidocrocite-like ferrititanate nanosheets and their full exfoliation with quaternary ammonium compounds, Mater. Des. 85 (2015) 197–204.

[27] N. Sakai, Y. Ebina, K. Takada, T. Sasaki, Electronic Band Structure of Titania Semiconductor Nanosheets Revealed by Electrochemical and Photoelectrochemical Studies, J. Am. Chem. Soc. 126 (2004) 5851–5858.

[28] H. Khan, I.K. Swati, Fe^{3+}-doped Anatase TiO_2 with d-d Transition, Oxygen Vacancies and Ti^{3+} Centers: Synthesis, Characterization, UV-vis Photocatalytic and Mechanistic Studies, Ind. Eng. Chem. Res. 55 (2016) 6619–6633.

[29] W. Choi, A. Termin, M.R. Hoffmann, The Role of Metal Ion Dopants in Quantum-Sized TiO_2: Correlation between Photoreactivity and Charge Carrier Recombination Dynamics, J. Phys. Chem. 98 (1994) 13669–13679.

[30] Y. Huang, Z. Ai, W. Ho, M. Chen, S. Lee, Ultrasonic Spray Pyrolysis Synthesis of Porous Bi_2WO_6 Microspheres and Their Visible-Light-Induced Photocatalytic Removal of NO, J. Phys. Chem. C. 114 (2010) 6342–6349.

[31] Y. Huang, Y. Liang, Y. Rao, D. Zhu, J. Cao, Z. Shen, W. Ho, S.C. Lee, Environment-Friendly Carbon Quantum Dots/$ZnFe_2O_4$ Photocatalysts: Characterization, Biocompatibility, and Mechanisms for NO Removal, Environ. Sci. Technol. 51 (2017) 2924–2933.

[32] Q. Zhang, Y. Huang, S. Peng, Y. Zhang, Z. Shen, J. Cao, W. Ho, S.C. Lee, D.Y.H. Pui, Perovskite $LaFeO_3$-$SrTiO_3$ composite for synergistically enhanced NO removal under visible light excitation, Appl. Catal. B Environ. 204 (2017) 346–357.

[33] E. Luévano-Hipólito, A. Martínez-de la Cruz, Q.L. Yu, H.J.H. Brouwers, Precipitation synthesis of WO_3 for NO_x removal using PEG as template, Ceram. Int. 40 (2014) 12123–12128.

[34] E. Luévano-Hipólito, A. Martínez-de la Cruz, Photooxidation of NO_x using scheelite-type ABO_4 (A = Ca, Pb; B = W, Mo) phases as catalyts, Adv. Powder Technol. 28 (2017) 1511–1518.

[35] M. Habran, K. Krambrock, M.E.H. Maia da Costa, E. Morgado, B.A. Marinkovic, TiO_2 anatase nanorods with non-equilibrium crystallographic {001}

facets and their coatings exhibiting high photo-oxidation of NO gas, Environ. Technol. (2017) 1–9.

[36] M. A. S. Abreu, E. Morgado, P.M. Jardim, B. A. Marinkovic, The effect of anatase crystal morphology on the photocatalytic conversion of NO by TiO_2-based nanomaterials, Cent. Eur. J. Chem. 10 (2012) 1183–1198.

[37] N.H. Nguyen, H. Bai, Photocatalytic removal of NO and NO_2 using titania nanotubes synthesized by hydrothermal method, J. Environ. Sci. 26 (2014) 1180–1187.

[38] F.L. Toma, G. Bertrand, D. Klein, C. Coddet, Photocatalytic removal of nitrogen oxides via titanium dioxide, Environ. Chem. Lett. 2 (2004) 117–121.

[39] J.C.-C. Yu, V.-H. Nguyen, J. Lasek, J.C.S. Wu, Titania nanosheet photocatalysts with dominantly exposed (001) reactive facets for photocatalytic NO_x abatement, Appl. Catal. B Environ. 219 (2017) 391–400.

[40] J.A. Mendoza, D.H. Lee, J.-H. Kang, Photocatalytic removal of gaseous nitrogen oxides using WO_3/TiO_2 particles under visible light irradiation: Effect of surface modification, Chemosphere. 182 (2017) 539–546.

[41] T. Giannakopoulou, I. Papailias, N. Todorova, N. Boukos, Y. Liu, J. Yu, C. Trapalis, Tailoring the energy band gap and edges' potentials of g-C_3N_4/TiO_2 composite photocatalysts for NO_x removal, Chem. Eng. J. 310 (2017) 571–580.

[42] C.-H. Huang, Y.-M. Lin, I.-K. Wang, C.-M. Lu, Photocatalytic Activity and Characterization of Carbon-Modified Titania for Visible-Light-Active Photodegradation of Nitrogen Oxides, Int. J. Photoenergy. 2012 (2012) 1–13.

[43] T. Giannakopoulou, N. Todorova, G. Romanos, T. Vaimakis, R. Dillert, D. Bahnemann, C. Trapalis, Composite hydroxyapatite/TiO_2 materials for photocatalytic oxidation of NOx, Mater. Sci. Eng. B. 177 (2012) 1046–1052.

[44] H. Wang, Y. Sun, G. Jiang, Y. Zhang, H. Huang, Z. Wu, S.C. Lee, F. Dong, Unraveling the Mechanisms of Visible Light Photocatalytic NO Purification on Earth-Abundant Insulator-Based Core-Shell Heterojunctions, Environ. Sci. Technol. 52 (2018) 1479–1487.

[45] Y. Li, Y. Sun, W. Ho, Y. Zhang, H. Huang, Q. Cai, F. Dong, Highly enhanced visible-light photocatalytic NO_x purification and conversion pathway on self-

structurally modified g-C_3N_4nanosheets, Sci. Bull. 63 (2018) 609–620.

[46] W. Cui, J. Li, Y. Sun, H. Wang, G. Jiang, S.C. Lee, F. Dong, Enhancing ROS generation and suppressing toxic intermediate production in photocatalytic NO oxidation on O/Ba co-functionalized amorphous carbon nitride, Appl. Catal. B Environ. 237 (2018) 938–946.

[47] P. Chen, F. Dong, M. Ran, J. Li, Synergistic photo-thermal catalytic NO purification of MnO_x/g-C_3N_4: Enhanced performance and reaction mechanism, Chinese J. Catal. 39 (2018) 619–629.

[48] F. Sannino, P. Pernice, C. Imparato, A. Aronne, G. D'Errico, L. Minieri, M. Perfetti, D. Pirozzi, Hybrid TiO_2–acetylacetonate amorphous gel-derived material with stably adsorbed superoxide radical active in oxidative degradation of organic pollutants, RSC Adv. 5 (2015) 93831–93839.

[49] T.W. Kim, H.W. Ha, M.J. Paek, S.H. Hyun, I.H. Baek, J.H. Choy, S.J. Hwang, Mesoporous iron oxide-layered titanate nanohybrids: Soft-chemical synthesis, characterization, and photocatalyst application, J. Phys. Chem. C. 112 (2008) 14853–14862.

[50] L. Wang, T. Sasaki, Titanium Oxide Nanosheets: Graphene Analogues with Versatile Functionalities, Chem. Rev. 114 (2014) 9455–9486.

[51] E. Scolan, C. Sanchez, Synthesis and Characterization of Surface-Protected Nanocrystalline Titania Particles, Chem. Mater. 10 (1998) 3217–3223.

[52] Y. Bai, Z. Xing, H. Yu, Z. Li, R. Amal, L. Wang, Porous Titania Nanosheet/Nanoparticle Hybrids as Photoanodes for Dye-Sensitized Solar Cells, ACS Appl. Mater. Interfaces. 5 (2013) 12058–12065.

[53] T. Gao, H. Fjellvåg, P. Norby, Raman Scattering Properties of a Protonic Titanate $H_xTi_{2-x/4}\square_{x/4}O_4\cdot H_2O$ ($\square$, vacancy; x = 0.7) with Lepidocrocite-Type Layered Structure, J. Phys. Chem. B. 112 (2008) 9400–9405.

[54] M.-J. Paek, H.-W. Ha, T.W. Kim, S.-J. Moon, J.-O. Baeg, J.-H. Choy, S.-J. Hwang, Formation Efficiency of One-Dimensional Nanostructured Titanium Oxide Affected by the Structure and Composition of Titanate Precursor: A Mechanism Study, J. Phys. Chem. C. 112 (2008) 15966–15972.

[55] E. Horváth, Á. Kukovecz, Z. Kónya, I. Kiricsi, Hydrothermal conversion of self-

assembled titanate nanotubes into nanowires in a revolving autoclave, Chem. Mater. 19 (2007) 927–931.

[56] S. Paek, H. Jung, Y. Lee, M. Park, S. Hwang, J.-H. Choy, Exfoliation and Reassembling Route to Mesoporous Titania Nanohybrids, Chem. Mater. 18 (2006) 1134–1140.

[57] I. Georgieva, N. Danchova, S. Gutzov, N. Trendafilova, DFT modeling, UV-Vis and IR spectroscopic study of acetylacetone-modified zirconia sol-gel materials, J. Mol. Model. 18 (2012) 2409–2422.

[58] I.Y. Kim, Y.K. Jo, J.M. Lee, L. Wang, S.J. Hwang, Unique advantages of exfoliated 2D nanosheets for tailoring the functionalities of nanocomposites, J. Phys. Chem. Lett. 5 (2014) 4149–4161.

[59] Q. Zhang, G. Rao, J. Rogers, C. Zhao, L. Liu, Y. Li, Novel anti-fouling Fe_2O_3/TiO_2 nanowire membranes for humic acid removal from water, Chem. Eng. J. 271 (2015) 180–187.

[60] S. Leytner, J.T. Hupp, Evaluation of the energetics of electron trap states at the nanocrystalline titanium dioxide/aqueous solution interface via time-resolved photoacoustic spectroscopy, Chem. Phys. Lett. 330 (2000) 231–236.

[61] J. Navío, G. Colón, M.I. Litter, G.N. Bianco, Synthesis, characterization and photocatalytic properties of iron-doped titania semiconductors prepared from TiO_2 and iron(III) acetylacetonate, J. Mol. Catal. A Chem. 106 (1996) 267–276.

[62] H. Deng, J.M. Hossenlopp, Combined X-ray Diffraction and Diffuse Reflectance Analysis of Nanocrystalline Mixed Sn(II) and Sn(IV) Oxide Powders, J. Phys. Chem. B. 109 (2005) 66–73.

[63] S. Larumbe, M. Monge, C. Gómez-Polo, Comparative study of (N, Fe) doped TiO_2 photocatalysts, Appl. Surf. Sci. 327 (2015) 490–497.

[64] B. Choudhury, A. Choudhury, Oxygen defect dependent variation of band gap, Urbach energy and luminescence property of anatase, anatase–rutile mixed phase and of rutile phases of TiO_2 nanoparticles, Phys. E Low-Dimensional Syst. Nanostructures. 56 (2014) 364–371.

[65] B. Xin, L. Jing, Z. Ren, B. Wang, H. Fu, Effects of Simultaneously Doped and Deposited Ag on the Photocatalytic Activity and Surface States of TiO_2, J. Phys.

Chem. B. 109 (2005) 2805–2809.

[66] J. Li, X. Yang, X. Yu, L. Xu, W. Kang, W. Yan, H. Gao, Z. Liu, Y. Guo, Rare earth oxide-doped titania nanocomposites with enhanced photocatalytic activity towards the degradation of partially hydrolysis polyacrylamide, Appl. Surf. Sci. 255 (2009) 3731–3738.

[67] H. Atout, M.G. Álvarez, D. Chebli, A. Bouguettoucha, D. Tichit, J. Llorca, F. Medina, Enhanced photocatalytic degradation of methylene blue: Preparation of TiO_2/reduced graphene oxide nanocomposites by direct sol-gel and hydrothermal methods, Mater. Res. Bull. 95 (2017) 578–587.

Supplementary Material

Visible light sensitive mesoporous nanohybrids of lepidocrocite-like ferrititanate coupled to a charge transfer complex: Synthesis, characterization and photocatalytic degradation of NO

Margarita Habran[1], Patricia I. Pontón[2], Lidija Mancic[3], Omar Pandoli[4], Klaus Krambrock[5], M. E. H. Maia da Costa[6], Sonia Letichevsky[1], Antonio M.L.M. Costa[1], Edisson Morgado Jr.[7], Bojan A. Marinkovic[1*].

[1]Department of Chemical and Materials Engineering, Pontifical Catholic University of Rio de Janeiro, 22451-900, Rio de Janeiro, RJ, Brazil, [2]New Materials Laboratory, Department of Materials, Escuela Politécnica Nacional, 170525, Quito, Ecuador, [3]Institute of Technical Sciences of SASA, Knez Mihailova 35/IV, Belgrade, Serbia, [4]Department of Chemistry, Pontifical Catholic University of Rio de Janeiro, 22451-900, Rio de Janeiro, RJ, Brazil, [5]Department of Physics, Federal University of Minas Gerais, 31270-901, Belo Horizonte, Brazil, [6]Department of Physics, Pontifical Catholic University of Rio de Janeiro, 22451-900, Rio de Janeiro, RJ, Brazil, [7] PETROBRAS S.A., Research & Development Centre, 21941-915, Rio de Janeiro, RJ, Brazil, *bojan@puc-rio.br.

S1.

Molar relationship between TBAOH and protonated lepidocrocite-like ferrititanate nanosheets (TBA^+/H^+).

$$\frac{0.27\ g_{TBAOH}}{259.47\frac{g}{mol_{TBAOH}}} = 0.001\ mol\ of\ \boldsymbol{TBAOH}$$

$$\frac{2.1\ meq}{100g} = 2.1 * 10^{-4}\ mol\ H^+\ for\ 1g\ of\ \boldsymbol{p-NS}$$

$$\frac{\boldsymbol{TBA^+}}{\boldsymbol{H^+}} = \frac{0.001\ \cancel{mol}}{2.1 * 10^{-4}\cancel{mol}} = 5$$

S2.

Calculation of chemical formula for $H_xTi_{2-x}Fe_xO_4 \cdot nH_2O$ (ferrititanate nanosheets).

ICP-AES results:

Fe = 24 % m/m ($\mathbf{X_{Fe}}$ =0.24)

Ti= 14.8 % m/m ($\mathbf{X_{Ti}}$ =0.14)

$$\boldsymbol{X_{Fe}} = \frac{MW_{Fe}}{MW_{Total}} = \frac{x\ MW_{Fe}}{MW_{Total}} = \frac{x(56)}{MW_{Total}} = 0.24$$

$$\boldsymbol{X_{Ti}} = \frac{MW_{Ti}}{MW_{Total}} = \frac{(2-x)\ MW_{Ti}}{MW_{Total}} = \frac{(2-x)(48)}{MW_{Total}} = 0.14$$

$$\frac{\boldsymbol{X_{Fe}}}{\boldsymbol{X_{Ti}}} = \frac{\frac{x(56)}{\cancel{MW_{total}}}}{\frac{(2-x)(48)}{\cancel{MW_{total}}}} = 1.62$$

$$\frac{X_{Fe}}{X_{Ti}} = \frac{x}{2-x} = 1.39$$
$$\frac{X_{Fe}}{X_{Ti}} = x = 2.78 - 1.39x$$
$$\frac{X_{Fe}}{X_{Ti}} = 2.39x = 2.78$$
$$x = 1.16$$

Thus, the chemical formula without considering the exact amount of water is $H_{1.16}Ti_{0.84}Fe_{1.16}O_4 \bullet nH_2O$ and molecular weight is 170.44 g mol^{-1}. The weight loss in the temperature range of 100-200ºC of dried p-NS observed curve TG is 1.8 wt% (see, fig 5 in reference [34]).

$$n\mathrm{H_2O} = \frac{170.44\,\frac{g}{mol}\,\mathrm{H_{1.16}Ti_{0.84}Fe_{1.16}O_4 \bullet nH_2O} * 100\,\%}{98.2\,\%} = 173.56\,\frac{g}{mol}$$

$n\mathrm{H_2O}$ = 3.12 g → Amount of water for=$H_{1.16}Ti_{0.84}Fe_{1.16}O_4 \bullet nH_2O$

$$n\mathrm{H_2O} = \frac{3.12\,g\,\mathrm{H_2O}}{18\frac{g}{mol}} = 0.17 \text{ mol } H_2O$$

Finally, chemical formula considering water is $H_{1.16}Ti_{0.84}Fe_{1.16}O_4 \bullet 0.17H_2O$ and its molecular weight is 173.56 g mol^{-1}.

S3.

Calculation of concentration of TiO_2-Acac in the as-synthesized TiO_2-sol.

$Ti(OiPr)_4$= 30 mL (density: 0.96 g mL^{-1} and molecular weight: 284.22 $gmol^{-1}$)

V_{total}= 20mL(Acac)+100mL(Ethanol)+30mL($Ti(OiPr)_4$)+180mL(H_2O+HNO_3)=330mL

$$30\,mL * 096\frac{g}{mL} = 28.8\ g\ \mathrm{Ti(OiPr)_4}$$

$$x = \frac{80\ \mathrm{g\ TiO_2} * 28.8\ \mathrm{g\ Ti(OiPr)_4}}{284\ \mathrm{g\ Ti(OiPr)_4}} = 8.11\ g\ TiO_2$$

$$x = \frac{8.11\ g\ \mathrm{TiO_2}}{80\frac{g}{mol}\ \mathrm{TiO_2}} = 0.101\ mol$$

$$[\mathrm{TiO_2}] = \frac{0.101 mol}{0.33 L} = 0.307 M$$

S4.

Complexant/metal (A), hydrolysis (H) and the acidity (H^+) ratios in the synthesized TiO_2-sol

Complexant/metal ratio (A):

$Ti(OiPr)_4$= 30 mL (density: 0.96 g/mL and molecular weight: 284.22 g/mol)

Acac= 20.38 mL (density: 0.97 g/mL and molecular weight: 100.13 g/mol)

Total Volume= 50.38 mL

Moles of $Ti(OiPr)_4$ in 30 mL:

$$30\ mL\ Ti(OiPr)_4 * \frac{0.96 g}{1 mL} * \frac{1\ mol}{284.22\ g} = 0.10\ mol\ Ti(OiPr)_4 = 0.1\ mol\ Ti$$

$$[Ti] = \frac{0.1\ mol}{50.38\ mL} * \frac{1000\ mL}{1 L} = 1.98\ M$$

Moles of Acac in 20.38 mL:

$$20.38\ \cancel{mL}\ Acac * \frac{0.975\cancel{g}}{1\cancel{mL}} * \frac{1\ mol}{100.13\ \cancel{g}} = 0.198\ mol\ Acac$$

$$[Acac] = \frac{0.198\ mol}{50.38\ \cancel{mL}} * \frac{1000\ \cancel{mL}}{1L} = 3.93\ M$$

A ratio:

$$A = \frac{[Acac]}{[Ti]} = \frac{3.93\ \cancel{M}}{1.98\ \cancel{M}} = 1.98$$

Hydrolysis ratio (H):

HNO_3 (density: 1.51 g/mL and molecular weight: 63.01 g/mol)

Water180 mL of a 0.015 M aqueous solution of HNO_3

Moles of HNO_3 in 180 mL of solution:

$$\frac{0.015\ mol\ HNO_3}{1\ \cancel{L}\ of\ solution} * 180\ \cancel{mL} * \frac{1\cancel{L}}{1000\ \cancel{mL}} = 0.0027\ mol\ HNO_3 = 0.0027\ mol\ H^+$$

$$0.0027\ \cancel{mol}\ HNO_3 * \frac{63.01\ \cancel{g}}{1\ \cancel{mol}} * \frac{1\ mL}{1.51\ \cancel{g}} = 0.112\ mL\ HNO_3$$

Moles of H_2O in 180 mL of solution:

Volume of water= 180-0.1126=179.89 mL

$$179.89\ \cancel{mL}\ H_2O * \frac{1\ \cancel{g}}{1\ \cancel{mL}} * \frac{1\ mol}{18\ \cancel{g}} = 9.99\ mol\ H_2O$$

Total volume= 50.38+180 mL=230.38 mL

$$[H_2O] = \frac{9.99\ mol}{230\ \cancel{mL}} * \frac{1000\ \cancel{mL}}{1\ L} = 43.43\ M$$

$$[Ti] = \frac{0.1\ mol}{230\ \cancel{mL}} * \frac{1000\ \cancel{mL}}{1\ L} = 0.435\ \text{M}$$

H ratio:

$$H = \frac{[H_2O]}{[Ti]} = \frac{43.43\ \cancel{M}}{0.435\ \cancel{M}} = 99.8$$

Acidity ratio [H^+]:

$$[H^+] = \frac{0.0027\ mol}{230\ \cancel{mL}} * \frac{1000\ \cancel{mL}}{1L} = 0.0117\ M$$

$$H = \frac{[H^+]}{[Ti]} = \frac{0.0117\ \cancel{M}}{0.435\ \cancel{M}} = 0.027$$

S5.

The adopted [Ti] anatase/[Ti] ferrititanate mol ratios for HM-2 and HM-1 respectively.

[Ti] anatase/[Ti] ferrititanate mol ratio for HM-2:

Moles of Ti in TiO_2-Acac-Sol (12 mL of 0.307 M solution)

$Ti(OiPr)_4$= 30 mL (density: 0.96 g mL^{-1} and molecular weight: 284.22 g/mol)

V_{total}= 20mL(Acac)+100mL(Ethanol)+30mL($Ti(OiPr)_4$)+180mL(H_2O+HNO_3)=330mL

$$30\cancel{mL} * 096\frac{g}{\cancel{mL}} = 28.8\ g\ Ti(OiPr)_4$$

$$x = \frac{48\ \text{g Ti} * 28.8\ \cancel{g\ Ti(OiPr)_4}}{284\ \cancel{g\ Ti(OiPr)_4}}$$

$x = 4.87\ g$ Ti of 330 mL

$$\frac{4.87\ \text{g Ti} * 12.01\ \cancel{\text{mL}}}{330\ \cancel{mL}} = 0.177\ g\ Ti$$

$$\frac{0.177\ \cancel{g}\ Ti}{48\frac{\cancel{g}}{mol}} = \mathbf{3.7 * 10^{-3}\ mol}$$

Moles of Ti in p-NS/TBA$^+$ (dispersion of 0.069 g of p-NS/TBA$^+$ in 40 mL of deionized water)

Weight loss in the temperature range < 200 °C for p-NS/TBA$^+$ slurry in the TG (fig S1) was determined as 58 wt%.

$$0.069\ g\ \text{H}_{1.16}\text{Ti}_{0.84}\text{Fe}_{1.16}\text{O}_4 \bullet 0.17\ \text{H}_2\text{O}\ _{(slurry)} * \frac{(100\% - 58\%)}{100\%} = 0.029 g\ \text{H}_{1.16}\text{Ti}_{0.84}\text{Fe}_{1.16}\text{O}_4$$

$$\frac{0.029\ g\ \cancel{\text{H}_{1.16}\text{Ti}_{0.84}\text{Fe}_{1.16}\text{O}_4} * (0.84 * 48)\frac{\cancel{g}}{\cancel{mol}}\ de\ Ti}{170.44\frac{\cancel{g}}{\cancel{mol}}\ \cancel{\text{H}_{1.16}\text{Ti}_{0.84}\text{Fe}_{1.16}\text{O}_4}} = 0.007\ g\ \ Ti$$

$$0.007\ \cancel{g}\ de\ Ti * \frac{1}{48\frac{\cancel{g}}{mol}} = \mathbf{1.4 * 10^{-4}\ mol\ of\ Ti}$$

[Ti] anatase/[Ti] ferrititanate mol ratio:

$$\frac{Ti_{Anatásio}}{Ti_{p-NF/TBA^+}} = \frac{3.7 * 10^{-3}\ \cancel{mol}\ Ti}{1.4 * 10^{-4}\ \cancel{mol}\ Ti} = \mathbf{26}$$

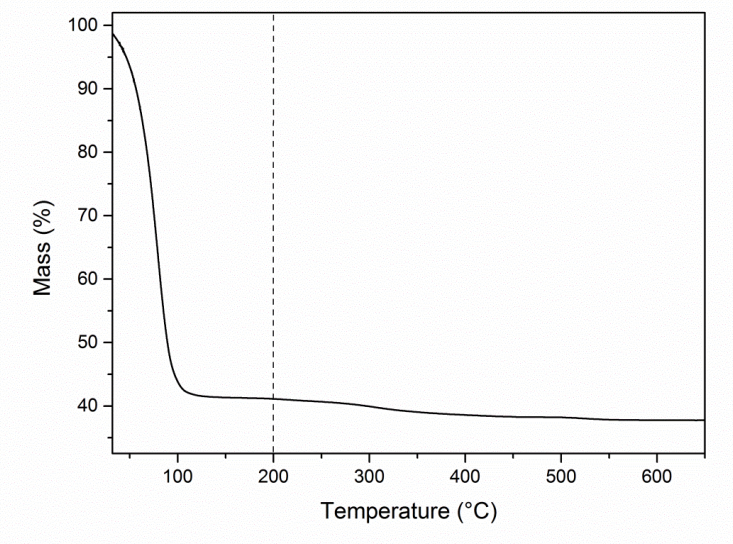

Figure S1. TGA curve of p-NS/TBA$^+$ slurry.

[Ti] anatase/[Ti] ferrititanate mol ratio for HM-1:

Moles of Ti in TiO_2-Acac-xerogel (dispersion of 0.286 g of TiO_2-Acac-xerogel in 8.8 mL of deionized water)

Weight loss in the temperature range 30 – 550 °C for TiO_2-xerogel was determined as 23.39 wt % by TG (fig 6).

$$0.286\ g\ * \frac{100\% - 23.39\%}{100\%} = 0.219\ g\ \ \text{Ti}O_2\text{-Acac}$$

$$\frac{0.219\ \cancel{g}\ TiO_2 - Acac}{80\ \frac{\cancel{g}}{mol}\ TiO_2 - Acac} = 2.7 * 10^{-3}\ mol\ \mathrm{Ti}O_2 - Acac$$

$$1\ \text{mol de Ti} \ - - - - - - - - - 1\ \text{mol de Ti}O_2 - Acac$$

$$X = \mathbf{2.7 * 10^{-3}\ mol\ of\ Ti}$$

Moles of Ti in p-NS/TBA$^+$ (dispersion of 0.069 g of p-NS/TBA$^+$ in 40 mL of deionized water)

Same procedure, described in the section S6 for HM-2

[Ti] anatase/[Ti] ferrititanate mol ratio:

$$\frac{Ti_{Anatásio}}{Ti_{p-NF/TBA^+}} = \frac{2.7 * 10^{-3}\ \cancel{mol}\ Ti}{1.4 * 10^{-4}\ \cancel{mol}\ Ti} = 19$$

S6.

2D AFM image of an exfoliated nanosheet and its hight profile.

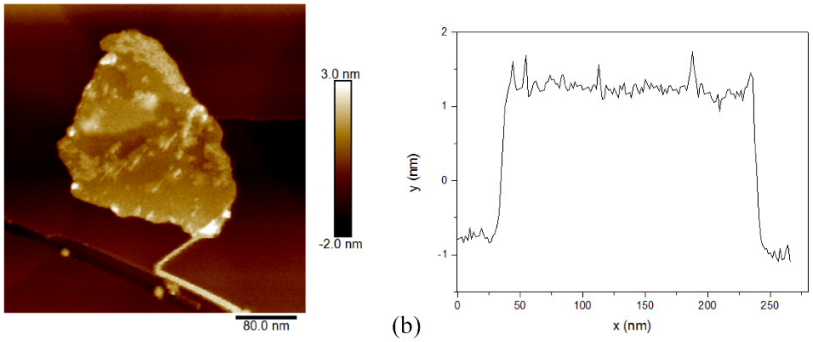

Figure S2- (a) 2D AFM image of an exfoliated nanosheet acquired by tapping mode in air and (d) its height profile.

S7.

Shows low temperature EPR spectra of P-TiO_2 sample under illumination with UVA light (375 nm). Three different EPR signals can be identified: (i) Single electron trapped oxygen vacancy hole centers (Setov), (ii) Ti^{3+} electron centers and surface O_2^- hole centers.

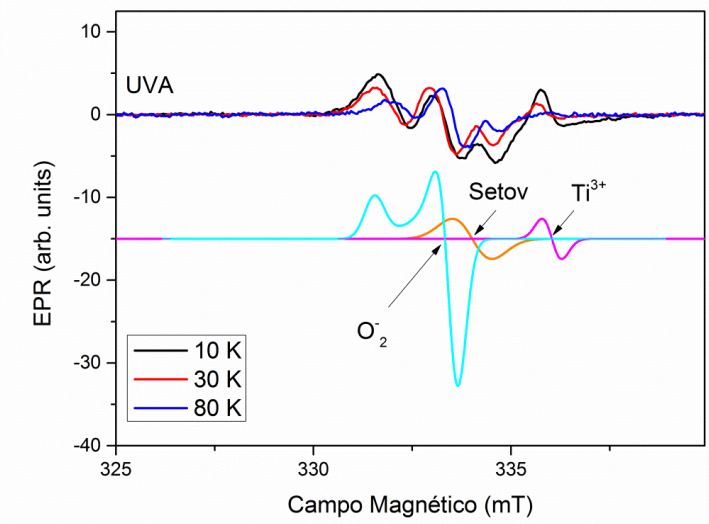

Figure S3-EPR spectra of NP-TiO_2-Acac sample under illumination with UVA light (375 nm) at low temperatures.

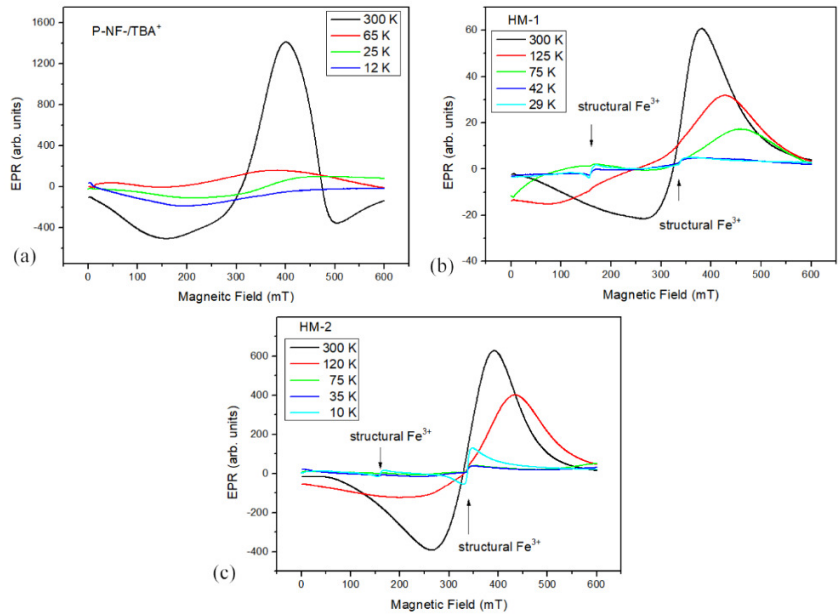

Figure S4-EPR spectra of samples p-NS/TBA+, MF, HM-1 and HM-2 measured at different temperatures.

S8.

FTIR curve of HM-1 and HM-2 before and after calcination at 300 °C.

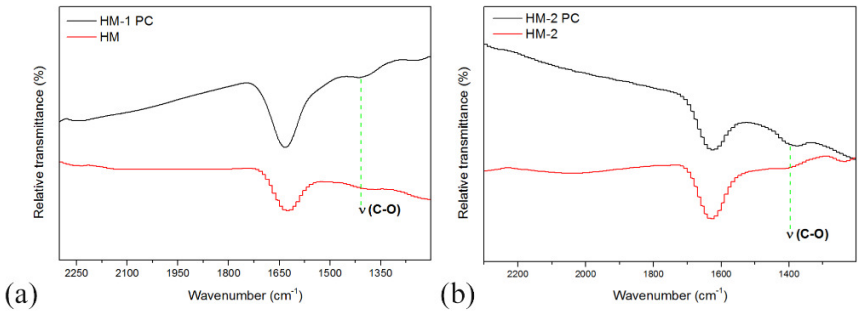

Figure S5-FTIR spectra of nanohybrids before and after calcination at 300°C: (a) HM-1 PC and HM-1, (b) HM-2 PC and HM-2.

S9.

TEM images of HM-1, HM-2 and HM-2 400°C.

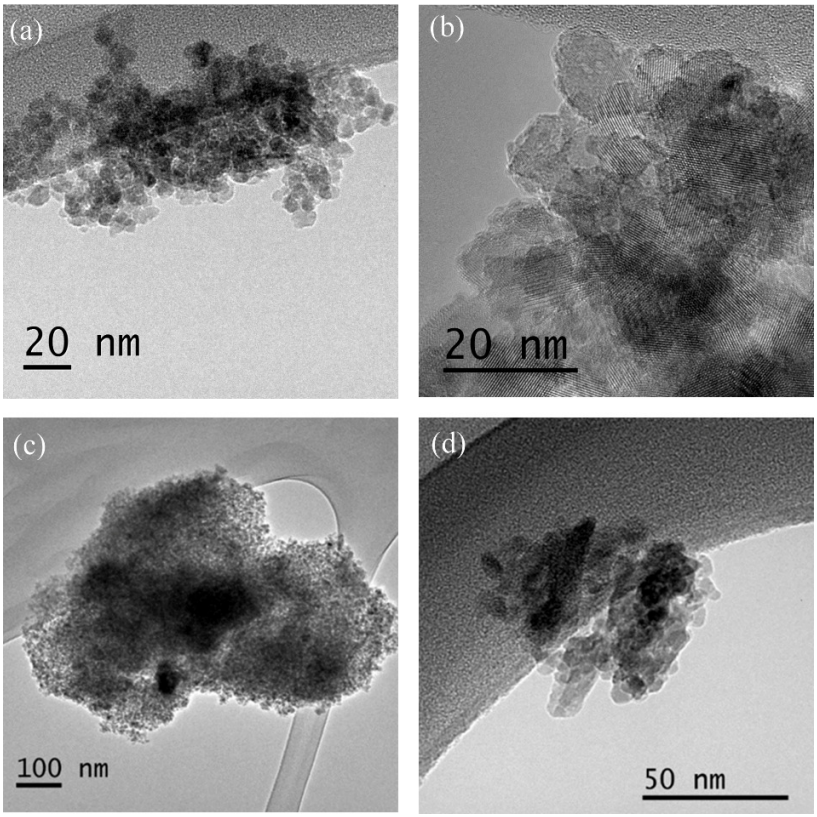

Figure S6-TEM images of (a) HM-2, (b) HM-2 400 °C, (c) HM-1 and (d) HM-2.

S10.

TEM images of HM-1

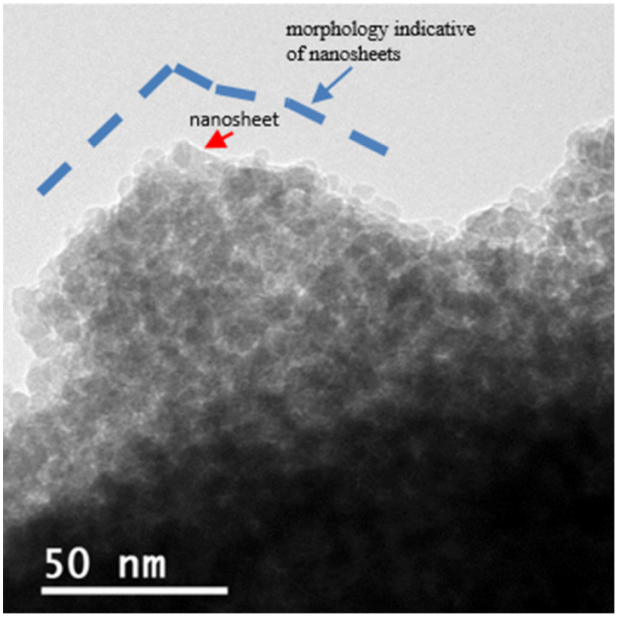

Figure S6-TEM image of a nanosheet in HM-1, supporting anatase nanoparticles.

S11.

XPS curves of HM-1 and HM-2.

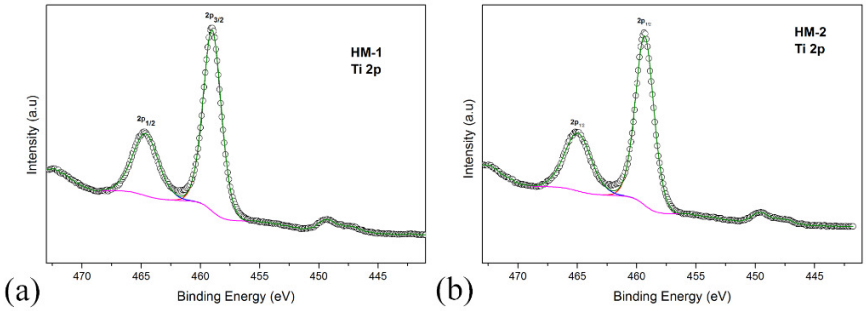

Figura S8-XPS spectra of the material (a)HM-1 and (b) HM-2.